Real-Time Monitoring and Prediction of Modes of Coherent Synoptic to Intraseasonal Tropical Variability

Matthew Wheeler*
National Center for Atmospheric Research,†Boulder, Colorado
Klaus M. Weickmann
NOAA-CIRES Climate Diagnostics Center, Boulder, Colorado

Submitted March 2000
Revised September 2000
2nd Revision January 2001

Monthly Weather Review

Corresponding author address: Dr. Matthew Wheeler, Bureau of Meteorology Research Centre, P.O. Box 1289K, Melbourne, 3001, Australia. E-mail: m.wheeler@bom.gov.au

†The National Center for Atmospheric Research is sponsored by the National Science Foundation.

ABSTRACT

A technique of near real-time monitoring and prediction of various modes of coherent synoptic to intraseasonal zonally-propagating tropical variability is developed. It involves Fourier filtering of a daily-updated global dataset for the specific zonal wavenumbers and frequencies of each of the phenomena of interest. The filtered fields obtained for times before the end of the dataset may be used for monitoring, while the filtered fields obtained for times after the end-point may be used as a forecast. Tests of the technique, using satellite-observed outgoing longwave radiation (OLR) data, reveal its skill for monitoring. For prediction, it demonstrates good skill for the Madden-Julian oscillation (MJO), and detectable skill for other convectively coupled equatorial modes, although the decaying amplitude of the predictions with time is a characteristic that users need to be aware of. The skill for the MJO OLR field appears to be equally as good as that obtained by the recent empirical MJO forecast methods developed by Waliser *et al.*, and Lo and Hendon, with a useful forecast out to about 15 to 20 days. Unlike the previously-developed methods, however, the current monitoring and prediction technique is extended to other defined modes of large-scale coherent zonally-propagating tropical variability. These other modes are those that appear as equatorial wave-like oscillations in the OLR. For them, the skill shown by this empirical technique, although considerably less than that obtained for the MJO, is still deemed to be high enough for the technique to be sometimes useful, especially when compared to that of a medium-range global numerical weather prediction (NWP) model.

1. Introduction

Since the pioneering work of Lorenz and others of the 1960s (e.g., Lorenz 1969), it is often generally accepted that the theoretical limit of predictability of synoptic-scale weather systems is on the order of a week or so, given the theoretical growth of baroclinic weather disturbances (see also Smagorinsky 1969; Lorenz 1982). In practice, however, useful skill in forecasts from current numerical weather prediction (NWP) models is often shorter due to the influence of inadequacies in the parameterization of various physical processes. This is especially the case in the tropics, due to the overwhelming influence of the diabatic heating of cumulus convection there (Tiedtke *et al.* 1988). Beyond this limit of useful skill provided by current NWP models, extended-range prediction of the weather is thought to rely, besides improvement and extension of the parameterizations and NWP-like models themselves, on the empirical exploitation of any lower-frequency periodicities, or quasi-periodicities, that exist in the atmosphere or land-ocean-atmosphere system (Palmer 1993; van den Dool 1994).

The idea behind such extended-range prediction is the intuitive notion that the predictability time of a phenomenon should be proportional to its own period or lifetime (e.g., van den Dool and Saha 1990). This notion has been the basis, for example, of the efforts made on the prediction of the interannual El Niño-Southern Oscillation (ENSO) phenomenon (e.g., Barnett *et al.* 1988). Yet there exist other low-frequency[1] quasi-periodic phenomena that have so far been much less, or not at all, utilized for prediction. Among them are the various synoptic to intraseasonal waves and oscillations that exist in the tropics (e.g., Madden and Julian 1994; Wheeler *et al.* 2000). Such waves and oscillations organize the individual mesoscale convective elements in the tropics on spatial scales that are larger ($\geq$ 1000 km) than the size of the elements themselves, with periods from a few days to a number of weeks. As such, they appear prominently in zonal wavenumber-frequency spectra of various proxies of the convection, cloud, and precipitation fields in the tropics (Salby and Hendon 1994; Wheeler and Kiladis 1999, hereafter WK99; see also Fig. 1), a fact that implies some potential for predictability. Yet the waves are not well simulated by NWP models (Waliser *et al.* 1999; Hendon *et al.* 2000; and references therein). We focus on these modes of variability in this study. In particular, we present a technique of (near) real-time monitoring and empirical prediction of such modes.

As labeled in Fig. 1, the modes of variability we are concerned with are the Madden-Julian

[1] We use the term low-frequency to refer to phenomena that have time scales that are longer than a few days, which is about the limit of useful skill of tropical precipitation forecasts from modern NWP models (this study; Krishnamurti *et al.* 1994).

oscillation (MJO), an eastward zonally-propagating signal discovered by Madden and Julian (1971), and various equatorial wave-like modes that also appear as zonally-propagating signals in tropical convection (e.g., Takayabu 1994; WK99). Of the latter, we examine the modes known as the convectively coupled Kelvin, $n = 1$ equatorial Rossby (ER), and mixed Rossby-gravity (MRG) waves. We do not concern ourselves with the convectively coupled inertio-gravity waves that exist at higher frequencies, nor do we consider other modes of tropical variability that may exist as non-zonally-propagating signals.

A review of the observations of the MJO is provided by Madden and Julian (1994). For the less well-known convectively coupled equatorial waves, a presentation of the observed three-dimensional structure is provided by Wheeler *et al.* (2000). From these observational studies, it is known that these modes of variability exist as large-scale coherent convective anomalies, propagating either to the east or west, coupled with the large-scale tropospheric circulation. They thus form an important part of the "weather" of the tropics, yet they also may drive teleconnections to the extratropics, impacting extratropical weather as well (e.g., Ferranti *et al.* 1990; Meehl *et al.* 1996).

Previous work on the empirical monitoring and prediction of such modes of tropical variability, to our knowledge, has been limited to the MJO. von Storch and Baumhefner (1991) developed a MJO forecast scheme based on principal oscillation pattern analysis of equatorial upper-tropospheric velocity potential. Waliser *et al.* (1999) developed a scheme based on singular value decomposition of lagged maps of intraseasonally filtered outgoing longwave radiation (OLR), an indicator of convection, and upper-level zonal wind. Most recently, Lo and Hendon (2000) developed a forecast scheme that predicts the evolution of the empirical orthogonal functions of OLR and upper-level streamfunction that describe the MJO. Basically, what all of these schemes have in common is their ability to identify the large-scale, low-frequency, circulation or convection anomalies associated with the MJO, and to propagate these large-scale anomalies slowly to the east as a forecast. The main hurdle for the use of these methods in real-time was considered to be the extraction of the low-frequency signals without the use of a low- or band-pass filter requiring information into the future. Useful forecast skill was thought to be achieved out to about 15 to 20 days, especially during times when the MJO was particularly active, and this skill surpassed that of various dynamical models, even for the large-scale circulation. Thus significant advantage was considered to be afforded by the use of such empirical forecast schemes, especially for the tropical regions that are directly affected by the MJO.

Here, we present another technique of monitoring and prediction of large-scale variations in the tropics. What sets the technique apart from those of the aforementioned studies, however, is

that we are able to apply it to all of the modes of variability that appear as spectral peaks in the wavenumber-frequency domain. This new technique involves Fourier filtering of a daily-updated global dataset for the specific zonal wavenumbers and frequencies of each of the phenomena of interest. The technique, and the data we use, are described in detail in Sections 2 and 3, followed by some examples in Section 4. Obviously, such one-sided filtering that includes the most recent day of data may involve spurious edge effects at the end of the dataset. Validation of the technique, and analysis of its forecast skill, are thus an important component of this study, and are presented in Section 5. Comparison of this skill is made to that of some of the previous studies, and in Section 6, comparison is made with forecasts derived from the National Center for Environmental Prediction (NCEP) Medium Range Forecast (MRF) model. A discussion and conclusions are presented in Section 7. Components of this research may also be viewed in (near) real-time on the World Wide Web as part of the NOAA-CIRES Climate Diagnostics Center "Map Room" at http://www.cdc.noaa.gov/map/clim/olr_modes/.

2. Data

In this study, we have chosen to concentrate on data that are representative of the moist convection and precipitation of the tropics. The reason is three-fold. First, precipitation has direct importance for the users of weather forecasts. Second, tropical precipitation has been notoriously difficult to represent and predict in NWP-like models. For example, Janowiak (1992) showed that certain NWP models do not correctly represent the temporal variations of rainfall in the tropics, even if the mean state appears adequate. And third, through satellite measurements, there are a good number of observations of proxies for precipitation that can be adequately used for our daily monitoring and prediction of the entire tropics. With this in mind, most of the results presented in this paper use the 2.5° gridded dataset of satellite-observed OLR as described by Liebmann and Smith (1996). Such data have often been used to distinguish areas of deep tropical convection and as a proxy for precipitation (e.g., Arkin and Ardanuy 1989). The OLR dataset now extends continuously for about two decades, and was the primary data used by WK99 to identify the spectral peaks of the modes of tropical variability (see Fig. 1). It is this dataset, in its daily-averaged form, and available in near real time, that forms the basis of our empirical monitoring and prediction scheme.

Other data to be used include precipitation output from some of the dynamic extended range forecasts (DERF) computed by the NCEP MRF model as described in Schemm *et al.* (1996). These are the same numerical model forecast experiments that were used by Waliser *et al.* (1999),

Lo and Hendon (2000), and Jones *et al.* (2000), although here we concentrate on the precipitation field,[2] as opposed to upper level winds. The forecast model is the T62L28 reanalysis version of the NCEP MRF model (Kalnay *et al.* 1996), for which 50-day forecasts were made each day from the 0Z reanalysis initial conditions. Sea surface temperatures in the model were prescribed at the lower boundary, and were damped to climatology from the observed initial condition with a 90-day e-folding time. For the purpose of comparison in this study, we use portions of these forecasts made for days within 1985 to 1988.

Also for the purpose of comparison, we additionally use the precipitation product from the satellite-borne Microwave Sounding Unit in this study (MSU; see Spencer 1993). The MSU precipitation dataset is available only over ocean, but is on the same 2.5° grid and daily-averaged like the OLR. The MRF model precipitation, on the other hand, required linear interpolation to be on the same 2.5° grid as the OLR and MSU, and its daily values are taken at 0Z, causing some ambiguity in the timing. Through these three datasets, we are able to capture an important component of the day-to-day weather variability of the real world and of a typical NWP model.

3. Formulation of technique

For the formulation of our technique of monitoring and prediction, we start with a recognition of the existence of various spectral peaks in the wavenumber-frequency domain that occur in the tropical convection or precipitation field. A representation of these spectral peaks, from WK99, is shown in Fig. 1. This figure, which was calculated using the OLR dataset (see WK99 for details), shows the spectral peaks that exist relative to a defined background spectrum. The left panel is for the antisymmetric (w.r.t. the equator) component, and the right panel is for the symmetric component, where the power was calculated independently at each latitude and then summed between 15°S and 15°N. The ratio of the raw power to the power of the defined smooth red background spectrum was then computed, as displayed. Contours of the ratio less than a value of 1.1 or greater than 1.4 are omitted. Thus each of the contoured spectral peaks have power that extends more than 10% above the background (i.e. a ratio of at least 1.1). Their statistical significance, considering the use of all data between 1979 and 1996, is also very high (95%, as estimated by WK99). Not surprisingly, very similar spectral peaks occur for a long time-series of the daily MSU precipitation data as well (not shown).

Based on the existence of these spectral peaks, the procedure of this study is to filter the constantly updated OLR for the various modes that produce the peaks, and to extend these filtered

[2]OLR was not available for the model forecasts.

fields into the future as a forecast. This filtering is performed for the specific zonal wavenumbers and frequencies enclosed by the boxed regions of Fig. 1. These regions are designed to enclose the spectral peaks of the disturbances. The boxes are drawn such that the outlines are inclusive, meaning that the wavenumber or frequency where the edge of the box is drawn is included in the filtered data. For the so-called convectively coupled equatorial waves (i.e., Kelvin, $n = 1$ equatorial Rossby, mixed Rossby-gravity) the boxed regions are also designed to lie along the theoretical dispersion curves (in an adiabatic, motionless basic sate), separately for the symmetric or antisymmetric components (see Matsuno 1966). For the MJO, on the other hand, the regions of filtering are for the box enclosing eastward moving wavenumbers 1–5 in *both* the antisymmetric and symmetric components, and for the frequency range from 1/96 cpd to 1/30 cpd. The two regions with notable spectral peaks at higher frequencies that are not enclosed by a boxed region are for the $n = 0$ eastward and $n = 1$ westward inertio-gravity waves, in the antisymmetric and symmetric components, respectively. We do not consider the inertio-gravity waves in this study.

For the filtering procedure, it should be noted that the regions of Fig. 1 are like those employed for filtering by WK99 (their Fig.6). Here, as in the previous study, filtering is performed using forward and inverse complex FFTs, independently at each latitude, retaining only those Fourier coefficients within each of the defined regions of filtering before the inverse FFTs. All coefficients outside the regions are assigned to be zero.

The filtering is performed on the OLR anomalies created by the removal of the long-term mean and first three harmonics of the seasonal cycle. Such filtering, when performed in conjunction with the separation of the OLR dataset into antisymmetric and symmetric components, successfully isolated the modes of concern in WK99. The geographical distribution of the variance of the filtered data, for example, matched the distribution expected from theory for the equatorial wave modes (see also Figs. 6, 11, 15, and 19 in this study), and some individual examples of the filtered anomalies successfully captured large-scale convective events evident in the total field. However, since the filtering in WK99 was designed as a diagnostic tool to be used well away from the temporal end-points of the dataset, and not for up-to-the-present monitoring or prediction, the dataset was tapered towards zero at each end to prevent spectral leakage. To adapt this technique for monitoring and prediction, we instead apply a taper only to the beginning of the OLR anomalies to be filtered, and pad the end of the dataset with over one year of zeroes. This allows the maximum amount of information to be retained at the end of the dataset, and as shown below, appears to work quite well. The zero-padding, on the other hand, is an important step to prevent information at the beginning of the dataset from distorting the signals produced by the filtering at the end. While we

have found that the results are generally insensitive to the length of the zero-padding employed, it is thought that at least several months is required to prevent this problem arising from the dataset periodicity that is assumed by the FFT. The padding also helps to increase the computational speed of the FFT, as it can be adjusted to allow the length of the dataset to be an integral power of 2. For example, using 1 year of the most recent actual data, plus 659 days of zero-padding, gives 1024 points in time[3]. Additionally, the 1 year of OLR anomalies has a linear least squares fit subtracted to remove any trend due to interannual variability before the filtering, and each day of gridded data is smoothed spatially by converting to spherical harmonics and applying a Rhomboidal truncation at wavenumber 21 (R21) to emphasize the larger-scale anomalies. This step of truncating to R21 effectively increases some measures of the apparent skill of the technique, yet it is not necessary for the success of the technique. Importantly, all of these steps for preparing the data for filtering can be performed in real time.

Fig. 2 presents a schematic of this procedure, as applied to the monitoring and prediction of a MJO-like signal. In this schematic, which shows the OLR data to be filtered at a single latitude/longitude location only, notice how the presence of a strong MJO-like signal near the end of the actual data continues as a signal in the filtered time series beyond the end-point of the dataset (i.e., into the zone that was padded with zeroes). Of course, this filtered signal is influenced by the presence or absence of an MJO-like signal at other longitudes as well. It is the part of the real-time filtered anomalies leading up to the end-point (i.e. "day 0") that we refer to as the real-time monitoring, while it is the part of the filtered data beyond day 0 that we use as a prediction. These predicted OLR anomalies are with respect to the seasonal cycle and any variability acting on longer time scales. In this schematic, they can be seen to decay towards zero rather rapidly beyond day 0. Such decay is a general property of all such forecasts, and will be discussed next. Further, although the schematic shows the forecast for a single mode of variability only, the real-time filtering procedure may efficiently produce a signal for each of the modes of variability labeled in Fig. 1. Such forecasts for each of the modes may be summed together, or used individually.

Evidently, the prediction component of this technique is rather unconventional, as it relies on how well (or rather, not well) the retained wavenumbers and frequencies approximate zero in the zero-padding region. The amplitude of the predicted signal is not only influenced by the presence of a strong wave-like signal at the end of the observed dataset, but is also influenced by the number of retained wavenumbers and frequencies for the mode of interest. At one extreme, if all the

[3]The technique was also tested using 5 years of the most recent actual data, plus 223 days of zero-padding, giving 2048 points in time. The results were virtually identical with those using 1 year of actual data.

wavenumbers and frequencies were retained (i.e. if the boxed region of filtering, as displayed in Fig.1, enclosed the *whole* region), then the predicted signal would exactly reproduce the zero-padding. At the other extreme, if only a single frequency was retained, then the predicted signal would be perfectly sinusoidal, and would maintain its (rather low) amplitude into the future. The technique of filtering we have described above lies between these two extremes, where we have set the width of each of the boxed regions of filtering in the wavenumber-frequency domain by the width of the observed spectral peaks in the OLR dataset. Thus the predicted signal by this technique decays with time, and this decay can be related to the statistical properties of the observed disturbances. For example, the width of the spectral peak of the MJO (as seen in detail in Salby and Hendon (1994)) is determined partly by the fact that MJO events often come in groups of only one, two, or three events at a time[4]. This localization of the MJO signal in time causes its spectral peak to be rather broad in frequency. Thus the decay of the predicted signal by this technique, which is related to the width of the MJO spectral peak in frequency, has, in part, a physical origin. Nevertheless, the utility of the technique requires extensive testing, including the decay of the amplitude of the predicted anomalies.

In subsequent sections, we will look at the predicted anomalies of the individual modes and compare them to both the total OLR field, and also to anomalies of the modes derived from the filtering when calculated using the dataset without nearby end-points (i.e. including a knowledge of the future, as in the filtering of WK99). We will refer to the latter as the "diagnostically-filtered" anomalies, while those of this new technique of monitoring and prediction (i.e. with an end-point) as the "real-time filtered" anomalies. Comparisons will also be made with verifying high-pass filtered OLR anomalies. Examples of the real-time filtering are provided next.

4. Examples

For examples, we concentrate on the time of the year around the onset of the southern hemisphere monsoon in southern equatorial latitudes. These examples come from the most recent few years, and do not necessarily represent either particularly strong or weak events of the various modes.

[4]The width of the spectral peak of the MJO is also determined by the range of speeds at which the MJO signal in OLR propagates to the east.

a. October-November-December 1996

Fig. 3a presents a time-longitude plot of the total OLR and filtered OLR for the MJO and $n = 1$ ER wave components for late 1996. The filtered fields of this first panel were calculated using the filtering on the whole dataset, that is, what we call the diagnostic filtering. Each of the fields are averaged between the latitudes of 10°S and 5°N to concentrate on the equatorial to southern equatorial convection. During this period, it can be seen that the convective variability was strongly influenced by disturbances like the "climatological" MJO and $n = 1$ ER waves, where the MJO is indicated by the planetary-scale features propagating to the east, and the ER waves are the slightly smaller-scale features propagating to the west. In particular, it appears that a combination of such disturbances was intimately involved in the timing and evolution of the most vigorous convection in the Australian-Indonesian region during early December.

It is now interesting to see how the real-time monitoring and prediction would have performed for these latitudes at this time. This is presented in Fig. 3b, where we have computed the real-time filtering with the end of the dataset on December 5th 1996. In this presentation, we have halved the contour interval of the plotted anomalies after day 0 due to the known decaying property of the predictions by the technique. Despite this decaying amplitude, however, we see that the technique performs quite well in this case at identifying the presence and phase of not only the mature wave-packet of ER waves, but also the development of the enhanced-convective phase of the MJO over the Indian Ocean in late November. The continuation of these filtered anomalies into the zero-padded region after the 5th also provides some good qualitative indications of the future behaviour of the convection out to about a forecast of 10 days or more. For example, at around 60°E on the 15th, the suppressed convection associated with the suppressed phase of the MJO is depicted well.

b. October-November-December-January 1997/98

Compared to the evolution of the convection in the latitudinal range of 10°S to 5°N during late 1996, that of late 1997 provides an interesting contrast. In Fig. 4a, as in Fig. 3a, we show the total OLR field averaged for these latitudes for this new period. As this period was during an ENSO warm event, the bulk of the convection is shifted into the central Pacific longitudes (the longitudes of the plot are also shifted by 40°). In addition, the synoptic to intraseasonal variability appears quite different, with the variations associated with the MJO (and ER waves) being weaker, and those of the convectively coupled Kelvin waves being stronger. This Kelvin wave variability is indicated quite well by the diagnostic filtering of Fig. 4a. In particular, there are events where the relatively fast eastward moving Kelvin waves propagate across the entire Pacific.

Turning now to the real-time filtering produced with the last day of data on January 5th (Fig. 4b), we see that the Kelvin wave filtering on this day provides some predictive value for equatorial South America by predicting an enhancement of convection there on about January 8th. For the real-time filtering of the MJO, on the other hand, the filtering predicts the suppressed convective phase around 120°E on January 10th, also quite consistent with what actually occurred.

c. November-December-January 1998/99

As a further example, the evolution of the convection during the 1998/99 season is displayed in Fig. 5. As in Figs. 3 and 4, we present a panel showing the total OLR and diagnostic filtering on the left, and a panel showing what the real-time filtering produced assuming a particular end of the dataset on the right. Only the MJO and convectively-coupled $n = 1$ ER waves appeared to significantly affect the evolution of the convection during this time, so only their filtered anomalies are shown. Of note is the only particularly strong enhanced-convective event of the MJO during this period, occurring in January, with the ER waves also reasonably strong at this time.

Looking at the real-time filtering as would have been produced with the end of the dataset on January 18th (Fig. 5b), we see that again the technique appears to be able to identify the modes of variability quite well. The continuation of the filtered anomalies into the future also does quite well at reproducing the phase of the anomalous component of the total OLR field, especially the envelope of enhanced convection associated with the MJO sweeping eastward toward 160°E by mid-February. Obviously, however, due to the zero-padding (of anomalies) employed, the predicted signals decay with time.

5. Validation and skill

Beyond showing such examples of our technique of monitoring and prediction, the technique may be more fully tested through a statistical analysis of multiple cases. Multiple cases of the real-time filtering have been generated by imposing end-points to the OLR dataset every second day for the 10-year period of 1985 to 1994, giving 1826 cases. We may then validate the technique by comparing the real-time filtered OLR with either the verifying diagnostically-filtered OLR (as calculated using the mode-specific wavenumber-frequency filtering without nearby end-points), or against a dataset of verifying high-pass OLR (i.e., like the diagnostically-filtered OLR, except including all wavenumbers, and all frequencies higher than the high-pass cut-off). A Lanczos filter of 301 weights was used for the high-pass filtering.

a. Madden-Julian oscillation (MJO)

Before analyzing the skill of the technique for monitoring and predicting the MJO, it is first useful to view maps of the part of the variance that we are attempting to explain by the MJO. Such maps are presented in Fig. 6, in the form of standard deviations, separately for southern summer (defined here as November to April) and Northern summer (May to October). These standard deviations were calculated from the diagnostically-filtered data for the same 10-year period for which we have made the multiple real-time filtering forecasts. Of note is the concentration of the MJO OLR variance in the southern hemisphere during southern summer, and the northern hemisphere during the opposite season, a well known feature of the observed MJO. It is this portion of the total variance of OLR that we are attempting to monitor and predict with the technique when applied to the MJO. This MJO standard deviation in OLR is quite similar, although of a slightly smaller magnitude, to that defined in the study of empirical prediction of Waliser *et al.* (1999) (their Fig. 13).

We now turn to Fig. 7 which shows maps of the correlations between the MJO real-time filtered OLR and the verifying diagnostically-filtered MJO OLR, for a number of lead times, where the lead time is with respect to the end-point of the data used for the real-time filtering. For example, the map for day -7 presents the correlation at each point between the real-time filtered OLR output 7 days before the imposed end-point, and the actual (diagnostically-filtered) OLR of the MJO that occurred on that day. This map at negative lag thus reflects the skill of the technique for real-time monitoring of the MJO. The maps at positive lag, on the other hand, reflect the performance of the real-time filtering as a prediction of the MJO, i.e., after the end-point. Note that although the diagnostically-filtered OLR that has been used for verification in this plot is a dataset that can only be produced after-the-fact, the predicted fields used in these correlations are a true indication of what could have been produced by this technique in an operational setting.[5] Also of note is that we are able to apply the technique to any season, thus we display the correlations here separately for southern summer (upper panels) and Northern summer (lower panels).[6] Given that 906 and 920 samples (spaced 2 days apart) went into these separate calculations of the correlations respectively, and that the autocorrelation of the MJO suggests that a more conservative estimate

[5]In this way, this technique has a practical advantage over that of Waliser *et al.* (1999), as, among other differences, Waliser *et al.* used bandpass filtered OLR as an input to their prediction scheme, which cannot be obtained in a true operational setting.

[6]In this way, this technique has at least one advantage over that presented in Lo and Hendon (2000), as, among other differences, they developed and applied their technique for southern summer only.

of the number of independent samples for these correlations is around 60 each (over the 10-year period), a correlation of 0.35 is significant at the 99% level. Thus almost all parts of the maps show correlations that are statistically significant.

Inspecting the maps of Fig. 7 further then, we see that the predictions of the MJO, by this measure of skill, perform best in the regions of the eastern Indian to western Pacific Oceans and South America south of the equator, in southern summer, and in the regions of the Indian Ocean and eastern Pacific, to the north of the equator, in Northern summer. Obviously, the skill reduces as one goes to longer lead forecasts, yet the 15-day forecasts show correlations greater than 0.6 over a broad region for Souther summer, and greater than 0.5 over a broad region for Northern summer. These correlations for the forecasts compare quite favorably with those calculated for the similar empirical prediction schemes of Waliser *et al.* (1999) (their Fig. 11) and Lo and Hendon (2000) (their Fig. 6). For a similar lead forecast of the MJO OLR, Waliser *et al.* (1999) obtained correlations of around 0.6 to 0.7, yet their forecasts could not be performed in real-time due to the band-pass filtering of predictors employed. Lo and Hendon (2000), on the other hand, obtained correlations of around 0.5 for 15-day forecasts of the leading principal components of OLR.

Fig. 7 further shows the correlations at negative lag. These correlations show that the real-time filtering field before the end-point is quite well-correlated (values generally greater than 0.8) with the diagnostically-filtered MJO field, especially in the regions where the MJO is strong (c.f. Fig. 6). Thus we feel that the technique is also quite adequate for real-time monitoring.

Given that the MJO is quite sporadic in nature, being identifiable in the observational record perhaps less than half of the time, it is also of interest to see how such correlations should change if calculated only for times when the MJO is determined to be active. We present such information in Fig. 8, in the form of the correlations as a function of lead time at a single point in the Timor Sea, together with the correlations at the same point for all seasons and southern summer for reference. Our definition of "active" is determined completely from the real-time filtered field, and is thus a decision that can be made in a true operational setting. It is simply based on whether the real-time filtered MJO field has a value of greater magnitude than 1.3 standard deviations at the point at any time from day -14 to day +14. This criterion retained 401 of the total 1826 values for the correlations. The predictions made at these times can be seen to be significantly improved, consistent with the results of the previous studies of von Storch and Baumhefner (1991) and Lo and Hendon (2000) that empirical forecasts of the MJO are much better at times when there is a large initial projection onto the MJO. The forecasts can also be seen to beat a persistence forecast of the diagnostically-filtered OLR after about 5 days (dotted line). The quick reduction of the

correlations for the persistence forecast to zero around day 12 to 13 reflects the MJO's time scale of around 50 days. Note that such a persistence forecast can not actually be performed in real time, as the diagnostically-filtered field uses information from the future.

Another way to look at the performance of the technique for real-time monitoring and prediction of the MJO is as shown in Fig. 9, in the form of the normalized root-mean-square (rms) errors relative to the diagnostically-filtered field. The rms errors are shown for the same point and seasons/periods as that used for presentation in Fig. 8, and are normalized by the standard deviation of the field that is being predicted (e.g. Fig. 6). As both the predicted and verifying fields are quite spatially coherent, such rms errors at a point are in fact representative of those over a fairly wide area. Knowing that the forecasts by the technique decay toward zero, their rms errors asymptote toward a value of 1, yet are at a value of only between 0.7 and 0.8 for a 10-day forecast. The rms errors of the persistence forecast, on the other hand, asymptote to $\sqrt{2}$, and they greatly exceed this value for 15- to 30-day forecasts due to the opposite phase of the MJO that tends to occur around that time. In comparison to the studies of Waliser *et al.* (1999) and Lo and Hendon (2000), these rms errors, like the correlations, are also quite favorable. For example, if the rms errors of the prediction technique of Waliser *et al.* are normalized (i.e. their Fig. 12 divided by their Fig. 13), one obtains values of around 0.7 to 0.8 for their 5- to 10-day forecasts.

A further, and more conservative, way to view the skill of the technique is via comparison with a verifying OLR field that includes all the synoptic to intraseasonal tropical variability. Fig. 10 shows such a comparison in the form of correlations of the MJO real-time filtered OLR with a 96-day high-pass OLR dataset. Obviously, the correlations are much lower than those presented in Fig. 7, as they are now an indication of the portion of the variance of the *total* synoptic to intraseasonal variability that is linearly accounted for by the real-time filtering. Such correlations, however, are no less statistically significant, and these correlations may also be compared to similar calculations presented by Waliser *et al.* (1999) and Lo and Hendon (2000) for their empirical prediction schemes (their Figs. 14 and 9 respectively). The regions where the forecasts perform best, and worst, are notably the same, and when one takes into account the 5-day means used for the comparison dataset by Waliser *et al.*, and the greater spatial smoothing of the comparison dataset employed by Lo and Hendon (they spectrally truncated their OLR dataset to T12), the magnitude of the correlations indicate that the current technique is equally as skillful. Consistently, the location and time of year for which 15-day forecasts by this technique are able to account for the largest portion of variance of OLR is in southern summer around the Timor Sea, and also in the region to the east of the Solomon Islands around 10°S, 170°E. There, the correlation coefficient of greater than 0.3

indicates that somewhat more than 9% of the variance of the daily-varying, 96-day high-pass, R21 spatially-truncated OLR dataset is accounted for by the 15-day forecasts in southern summer.

Also of note is that the correlations as presented in Figs. 7, 8, and 10 are appreciably higher than what are obtained if the same procedure of real-time filtering is performed for an equivalent region of the wavenumber-frequency domain that is characterized more by red-noise, that is, a region of the wavenumber-frequency domain of Fig. 1 that does not contain a spectral peak (not shown). Hence the success of the technique for the MJO is not just a statistical artifact, but relies on the existence of the MJO as a quasi-periodic phenomenon in the first place.

b. $n = 1$ equatorial Rossby (ER) wave

Turning now to the $n = 1$ ER waves, Fig. 11 displays the geographical distribution of their standard deviation. Compared to the standard deviation of the MJO (Fig. 6), the $n = 1$ ER waves can be seen to have less variance, with the local maxima being off the equator around 10°N and 10°S. By design of the filtering (e.g. Fig. 1), this standard deviation is also symmetric about the equator. It can also be seen that the $n = 1$ ER waves tend to be stronger in southern summer.

Concentrating on southern summer, the performance of the real-time filtering technique for monitoring and prediction of the $n = 1$ ER wave can be ascertained from Fig. 12. For a 6-day forecast, these correlations against the diagnostically-filtered $n = 1$ ER wave OLR are greater than 0.6 over four off-equatorial regions. These regions are around 10°N and S in the far western Pacific, and also over the far western Indian Ocean to eastern Africa. Based on a conservative estimate of 90 degrees of freedom (dof), a correlation of 0.27 is statistically significant at the 99% level, thus this apparent skill is quite significant. Compared to the correlations of the MJO in Fig. 7, however, these correlations show that the technique for the $n = 1$ ER wave for a 6-day forecast is only about as skillful as the technique is for a 15-day forecast of the MJO. Obviously, as the $n = 1$ ER waves have a shorter time scale than the MJO, they cannot be predicted as far in advance, consistent with the study of midlatitude variability of van den Dool and Saha (1990).

The other measure of skill that we use in this study, that is, the normalized rms error, is displayed for the real-time filtering of the $n = 1$ ER wave in Fig. 13. These rms errors are displayed for the point at 10°N, 140°E, and show the errors separately for all seasons, southern summer only, and for certain defined active periods of the $n = 1$ ER waves. These active periods were selected based on the magnitude of the real-time filtered field between day -8 and day +8, and retained 668 of the total 1826 forecasts made. For the predictions made with the technique during these active periods, a normalized rms error of 0.8 is not reached until about the 7-day forecast. Such an error is

far less than that obtained for a similar-lead forecast using persistence of the diagnostically-filtered $n = 1$ ER wave as a prediction (shown as the dotted line).

We also show a more conservative estimate of the skill of the technique for the $n = 1$ ER wave in Fig. 14. As in Fig. 10 for the MJO, this figure shows the correlations for the real-time filtering of the $n = 1$ ER wave when compared to an OLR field that contains a more complete spectrum of variance. The OLR field we compare to is the 40-day high-pass OLR, which contains all the variability of the total OLR field on time scales from daily up to a period around the maximum of that of the $n = 1$ ER wave. Unlike the maps of Fig. 12, these maps are not purely symmetric about the equator since the 40-day high-pass field is not symmetric. Correlations of the real-time filtered field against this field are on the order of 0.1 to 0.3 for the 6-day forecast across the western Pacific and central Indian Ocean regions. Also of note, however, are a few regions of negative correlation, indicating that the real-time filtered $n = 1$ ER wave component was a particularly bad forecast of the synoptic to intraseasonal variability in these regions.

c. Kelvin wave

Maps of the standard deviation of the diagnostically-filtered Kelvin wave field are displayed in Fig. 15. As can be seen, the variance of these waves in OLR is mostly confined to within about 10° latitude of the equator, and is spread more evenly with longitude than that for the MJO or $n = 1$ ER waves. It is this portion of the total synoptic to intraseasonal variance that we are attempting to monitor and predict when we apply the real-time filtering technique to the Kelvin wave region of the wavenumber-frequency spectrum.

Given that the seasonal cycle of the Kelvin wave variance is not very pronounced, we next look at an indicator of the skill of the technique for the Kelvin wave for all seasons (Fig. 16). As for the other waves, this figure shows correlations between the real-time filtered data and the diagnostically-filtered data for the Kelvin wave for a number of lead and lag times. These correlations can be seen to be maximized on the equator, and show that the technique performs best for the Kelvin wave in the region of the central to eastern Pacific for which the correlations are greater than 0.4 for the 4-day forecasts.

Looking at the rms errors for a point in the eastern Pacific in Fig. 17, we see that the skill of the technique for the Kelvin wave, like for the other waves, may also be improved by concentration on active periods of the waves. These active periods were chosen based on times when the real-time filtered field exceeded a threshold of 1.4 times the standard deviation at the point for any lead or lag time between ±5 days. This retained 491 samples for the calculation of the rms error. For the

Kelvin wave during active periods at this location, a normalized rms error of 0.8 is exceeded for the 3-day forecast. Thus the performance of the technique of real-time filtering dwindles much more quickly for the Kelvin wave than for the MJO or $n = 1$ ER wave.

A further view of the skill of the technique is presented in Fig. 18, which shows correlations between the real-time filtered Kelvin wave forecasts and a 30-day high-pass OLR field. These correlations are thus an indication of how much of the total synoptic to intraseasonal variability, excluding that of the MJO, the Kelvin wave forecasts account for at each point. Obviously, the forecasts with the Kelvin wave only produce useful information within about 10° latitude of the equator. Outside this latitude range the forecasts (i.e. the maps at positive lag) are mostly negatively correlated with the verifying 30-day high-pass OLR field. For the 4-day forecasts, relatively large areas of correlation of greater than 0.1 are seen only over the equatorial eastern Pacific and Africa. Given a conservative estimate of 800 dof for this calculation, these correlations are still statistically significant at the 99% level at 4 or 5 days. The range considered to be 'useful' by an operational forecaster, however, would no doubt be less, but even a useful 1- or 2-day forecast is still better than that which is often obtained for precipitation by NWP models in these regions (e.g., Krishnamurti *et al.* 1994; Janowiak 1992; next section).

d. Mixed Rossby-gravity (MRG) wave

As for the other waves, we display figures of the MRG wave standard deviation, and those showing the skill of the technique for monitoring and predicting the MRG wave, in Figs. 19 to 22. Previous studies have shown that these waves tend to have maximum amplitude during Northern fall (e.g., Hendon and Liebmann 1991), so we concentrate on this season.

The maximum OLR variance of this wave can be seen to be located near the date line at 7.5°N and 7.5°S (Fig. 19). The skill of predictions of this wave, however, when compared to the diagnostically-filtered field, are maximized somewhat to the east of this location (Fig. 20). These correlations are greater than 0.6 for a 4-day forecast, seemingly better than that for the Kelvin wave for the same lag forecast (Fig. 16).

As with the other modes studied in this paper, the skill of the technique for monitoring and prediction is improved for the MRG wave when concentrating on active periods of this wave (Fig. 21). These active periods were chosen in a similar way as for the other modes, a choice that can be made in real time. The normalized rms error calculated for the 438 points retained for the active periods does not exceed 0.8 until the 4-day forecast at the point displayed in Fig. 21. This measure of the skill of the technique also appears better than that for the Kelvin wave (Fig. 17).

Finally, a more conservative estimate of the skill of the technique for the MRG wave is displayed in Fig. 22 in the form of correlations of the real-time filtered field at various lags against a verifying 7-day high-pass OLR field. This figure shows that the real-time monitoring of the MRG wave locally accounts for the greatest portion of the 7-day high-pass variance in the regions of the Bay of Bengal, and the central Pacific to the north of the equator. Although such correlations can be determined to be statistically significant, the small amount of variance accounted for suggests that the technique when applied to the MRG wave would provide only quite minimal operational usefulness. Nevertheless, such forecasts of the convective activity associated with MRG waves may still at times be better than that obtained by a modern NWP model, as demonstrated in the next section.

6. Comparison with NWP model

To further assess the usefulness of the real-time filtering of the modes of variability for prediction, we compare the OLR forecasts of the real-time filtering with forecasts obtained from the NCEP MRF model. As longwave radiation data was not available from the model, however, we use precipitation data from the model. This is an extreme test of the model as tropical precipitation and clouds have been notoriously difficult to represent and predict in such models. Of course, the MRF model theoretically provides a prediction of all resolvable time and space scales, which may include not only the modes of variability we are concerned with in this study, but other tropical variability as well, including the variety of phenomena that constitute the red-noise background spectrum (e.g. tropical depressions, cold surges, tropical cyclones). For this reason we concentrate on two cases in which two of the modes were particularly strong and observable in the total OLR field, and thus theoretically possible to observe in unfiltered data from the MRF model as well. Note that such cases will shed the best possible light upon the usefulness of the real-time filtering because, as already shown, forecasts with this real-time filtering technique perform best when the modes are strong. The two cases are for a period of MJO events in late 1987 to early 1988 (Fig. 23), and for a period of convectively coupled MRG waves in April-May 1985 (Fig. 24).

The first panel of Fig. 23 (panel (a)) shows the total OLR field along with contours of the diagnostically-filtered MJO OLR for a 5-month period. The presence of MJO events is easily discerned in the unfiltered field at this time. Panel (b) shows a sequence of 5-day forecasts made with the real-time filtering technique that verify at the time as specified. Comparing the contours of the forecasted anomalies with the position of the contours of the verifying fields in panel (a), one can see that the 5-day forecasts from the real-time filtering perform quite well at predicting

the phase of the MJO events, although the amplitude of the predicted anomalies is about half that of the verifying anomalies. As discussed in Section 3, the reduced amplitude of the predicted anomalies is a known characteristic of this technique, and is also a trait of the previous empirical MJO prediction techniques of Waliser *et al.* (1999) and Lo and Hendon (2000). This reduced amplitude of predicted anomalies is further evident in panel (c) showing a sequence of the 15-day forecasts with the technique. The predicted phase of the anomalies, however, is still quite good, although there are some times during which the forecasts are slightly leading or lagging the verification field.

Panel (d) of Fig. 23 shows the MSU-derived precipitation for this same 5 month period. Noting that this observed precipitation field shows very similar variability to the observed OLR (panel (a)), we may then compare the real-time filtering forecasts to those of precipitation of the MRF model (panels (e) and (f)). The 5-day forecasts (panel (e)) shows some evidence of the intraseasonal MJO variability, presumably due to the existence of such variability in the initial conditions, but the 15-day forecasts (panel(f)) show no evidence of the MJO variability at all. Instead, the significant precipitation in the model shows a tendency to accumulate near the island of Papua New Guinea. This result is consistent with that of Hendon *et al.* (2000) that the MRF model is not able to sustain the slowly-varying anomalies associated with the MJO beyond about a 7-day forecast, even if the MJO is strongly present in the initial conditions. Knowledge of the future MJO progression provided by the real-time filtering is obviously of greater benefit during this period.

Turning now to a case of strong MRG waves appearing in the OLR and precipitation fields of the Pacific ITCZ (panels a and c of Fig. 24 respectively), we see that the MRG wave real-time filtering 2-day forecasts (panel (b)) provide a good qualitative prediction of this westward propagating synoptic-scale variability, especially during the later stages of the wave packet. The 2-day precipitation forecasts of the MRF model (panel (d) of Fig. 24), on the other hand, did not capture this variability with a near 5-day period. Thus again we are able to present a case, even for relatively short range forecasts (2 days), in which the predictions provided by the real-time filtering of a known mode of variability are able to out-perform a modern NWP model.

7. Summary and discussion

In this study, we have presented a technique of monitoring and prediction of various modes of coherent synoptic to intraseasonal zonally-propagating tropical variability which we apply to observed OLR data. The modes of variability considered are the MJO, and the convectively coupled $n = 1$ ER, Kelvin, and MRG waves. The technique demonstrates good predictive skill for the

MJO, and notable skill for the other convectively coupled equatorial modes. Compared to the previously-developed methods of empirical prediction of such modes of variability (i.e., von Storch and Baumhefner 1991; Waliser *et al.* 1999; Lo and Hendon 2000), the technique's strength is that it is possible to apply to any mode that appears as a significant spectral peak in the wavenumber-frequency spectrum, and not just the MJO. The technique can also be applied in near real time, and the same procedure may be used in any season. It is also conceptually simple, exploiting the method of Fourier filtering of the particular wavenumbers and frequencies of the modes. Further, the technique's skill for the MJO appears to be as equally as good as that of the previously developed methods. As with these previous methods, however, the decay of the amplitude of the forecasts is a characteristic of the technique that a user needs to be aware of.

With a mind toward the application of the technique for operational monitoring and prediction, the maps of correlations presented in this paper, especially those against a high-pass filtered field (Figs. 10, 14, 18, and 22), may be used as an indication of where and when the technique typically works, and does not work. At locations where the technique shows positive correlations at positive lags, the technique typically beats a persistence forecast (see rms errors in Figs. 9, 13, 17, and 21). More importantly, however, is that the technique (on OLR) is also able to, at least occasionally, beat (in terms of phase) forecasts produced by the NCEP MRF model (of precipitation). This is particularly the case during times when the modes of variability are quite active (e.g. Figs. 23 and 24). Part of the reason for this relatively poor performance of the MRF model is its inability to adequately simulate the modes of variability, as has been demonstrated for the MJO by Jones *et al.* (2000), and as will be demonstrated for the convectively coupled equatorial waves in a future paper. Early results show that its simulated convectively coupled equatorial waves are too high in frequency. Another part of the reason is likely related to inadequate initial conditions, especially in the equatorial regions that are not covered by the conventional observations (winds, temperatures, and humidities) that are ingested into the model.

Future improvement of the empirical technique may come with an alteration of the regions of filtering, as presented in their current form in Fig. 1. For example, it may be found that the long-range predictions of the MJO may be able to account for more variance by the inclusion of wavenumber-0 in its region of filtering. So far we have done little experimentation with the regions of filtering, except to discover that the technique does not provide a useful prediction (relative to persistence) if applied to a region of the wavenumber-frequency domain that does not contain a spectral peak (not shown). Experimentation has been performed, however, with the length of the zero-padding and the length of the actual data input to the FFTs. Relatively little difference was

found between using 5 years of actual data and 7 months of zero-padding compared to the 1 year of actual data and 659 days of zero-padding that we eventually employed for the multiple forecasts (see also Section 3).

Finally, while this and other empirical techniques show some promise for use by forecasters in the tropics, eventually it is hoped that predictions by NWP models should be able to surpass them. The current empirical schemes, for example, while generally good for predictions of the phase of the wave modes, suffer from problems in predicting the amplitude. As a consequence, predictions of extratropical teleconnections are even more problematic. NWP models may be able to improve this aspect of the predictions. After-all, an empirical scheme cannot match the ability of NWP models to take into account the effects of the full three-dimensional basic state (see also Meehl *et al.* 2000). Improvement of the NWP models ability to simulate the various modes of tropical variability is paramount for this future goal.

Acknowledgements

We thank Katherine Harris, George Kiladis, Roland Madden and Jerry Meehl for reading and providing beneficial comments on various versions of this manuscript. The revised manuscript also benefited from stimulating conversations with Harry Hendon, the comments of several anonymous reviewers, and some words of wisdom from the editor, Dave Raymond. Thanks also to Joan Hart of NOAA CDC for her assistance on the automation of the code for the daily monitoring, to John Janowiak of NCEP for providing the OLR data daily-updates, and to Jae Schemm for allowing our use of the NCEP DERF precipitation forecasts. All other data used in this study were obtained from NOAA CDC through their data archives (http://www.cdc.noaa.gov), and we thank the Climate and Global Dynamics Division of NCAR for the use of their computers.

REFERENCES

Arkin, P. A., and P. E. Ardanuy, 1989: Estimating climatic-scale precipitation from space: A review. *J. Climate*, **2**, 1229–1238.

Barnett, T., N. Graham, M. Cane, S. Zebiak, S. Dolan, J. O'Brien, and D. Legler, 1988: On the prediction of the El Niño of 1986–1987. *Science*, **241**, 192–196.

Ferranti, L., T. N. Palmer, F. Molteni, and E. Klinker, 1990: Tropical-extratropical interaction associated with the 30–60 day oscillation and its impact on medium and extended range prediction. *J. Atmos. Sci.*, **47**, 2177–2199.

Hendon, H. H., and B. Liebmann, 1991: The structure and annual variation of antisymmetric fluctuations of tropical convection and their association with Rossby-gravity waves. *J. Atmos. Sci.*, **48**, 2127–2140.

———, ———, M. Newman, and J. D. Glick, 2000: Medium Range forecast errors associated with active episodes of the Madden-Julian oscillation. *Mon. Wea. Rev.*, **128**, 69–86.

Janowiak, J. E., 1992: Tropical rainfall: A comparison of satellite-derived rainfall estimates with model precipitation forecasts, climatologies, and observations. *Mon. Wea. Rev.*, **120**, 448–462.

Jones, C., D. E. Waliser, J.-K. E. Schemm, and K.-M. Lau, 2000: Prediction skill of the Madden and Julian oscillation in dynamical extended range forecasts. *Climate Dyn.*, **16**, 273–289.

Kalnay, E., M. Kanamitsu, R. Kistler, W. Collins, D. Deaven, L. Gandin, M. Iredell, S. Saha, G. White, J. Woollen, Y. Zhu, M. Chelliah, W. Ebisuzaki, W. Higgins, J. Janowiak, K. C. Mo, C. Ropelewski, J. Wang, A. Leetmaa, R. Reynolds, R. Jenne, and D. Joseph, 1996: The NCEP/NCAR 40-year Reanalysis Project. *Bull. Amer. Meteor. Soc.*, **77**, 437–471.

Krishnamurti, T. N., G. D. Rohaly, and H. S. Bedi, 1994: On the improvement of precipitation forecast skill from physical initialization. *Tellus*, **46A**, 598–614.

Liebmann, B., and C. A. Smith, 1996: Description of a complete (interpolated) outgoing longwave radiation dataset. *Bull. Amer. Meteor. Soc.*, **77**, 1275–1277.

Lo, F., and H. H. Hendon, 2000: Empirical extended-range prediction of the Madden-Julian oscillation. *Mon. Wea. Rev.*, **128**, 2528–2543.

Lorenz, E. N., 1969: The predictability of a flow which possesses many scales of motion. *Tellus*, **21**, 289–307.

———, 1982: Atmospheric predictability experiments with a large numerical model. *Tellus*, **34**, 505–513.

Madden, R. A., and P. R. Julian, 1971: Detection of a 40-50 day oscillation in the zonal wind in the tropical Pacific. *J. Atmos. Sci.*, **28**, 702–708.

———, and ———, 1994: Observations of the 40-50-day tropical oscillation - A review. *Mon. Wea. Rev.*, **122**, 814–837.

Matsuno, T., 1966: Quasi-geostrophic motions in the equatorial area. *J. Met. Soc. Japan*, **44**, 25–43.

Meehl, G. A., G. N. Kiladis, K. M. Weickmann, M. Wheeler, D. S. Gutzler, and G. P. Compo, 1996: Modulation of equatorial subseasonal convective episodes by tropical-extratropical interaction in the Indian and Pacific Ocean regions. *J. Geophys. Res.*, **101**, 15,033–15,049.

———, R. Lukas, G. N. Kiladis, K. M. Weickmann, A. J. Matthews, and M. Wheeler, 2000: Time and space scale interactions in the climate system: Implications for climate variability and predictability. *Climate Dyn.*, accepted.

Palmer, T. N., 1993: Extended range atmospheric prediction and the Lorenz model. *Bull. Amer. Meteor. Soc.*, **74**, 49–66.

Salby, M. L., and H. H. Hendon, 1994: Intraseasonal behaviour of clouds, temperature and motion in the Tropics. *J. Atmos. Sci.*, **51**, 2207–2224.

Schemm, J. E., H. M. van den Dool, and S. Saha, 1996: A multi year DERF experiment at NCEP. *Preprints, 11th Conference on Numerical Weather Prediction*, Norfolk, VA. Amer. Meteor. Soc.. 47–49.

Smagorinsky, J., 1969: Problems and promises of deterministic extended range forecasting. *Bull. Amer. Meteor. Soc.*, **50**, 286–311.

Spencer, R. W., 1993: Global oceanic precipitation from the MSU during 1979–1991 and comparisons to other climatologies. *J. Climate*, **6**, 1301–1326.

Takayabu, Y. N., 1994: Large-scale cloud disturbances associated with equatorial waves. Part I: Spectral features of the cloud disturbances. *J. Met. Soc. Japan*, **72**, 433–448.

Tiedtke, M., W. A. Heckley, and J. Slingo, 1988: Tropical forecasting at ECMWF: The influence of physical parameterization on the mean structure of forecasts and analyses. *Quart. J. Roy. Meteor. Soc.*, **114**, 639–664.

van den Dool, H. M., 1994: Long-range weather forecasts through numerical and empirical methods. *Dyn. Atmos. Ocean*, **20**, 247–270.

———, and S. Saha, 1990: Frequency dependence in forecast skill. *Mon. Wea. Rev.*, **118**, 128–137.

von Storch, H., and D. P. Baumhefner, 1991: Principal Oscillation Pattern analysis of the tropical 30–60 day oscillation. Part II: The prediction of equatorial velocity potential and its skill. *Climate Dyn.*, **6**, 1–12.

Waliser, D. E., C. Jones, J.-K. E. Schemm, and N. E. Graham, 1999: A statistical extended-range tropical forecast model based on the slow evolution of the Madden-Julian oscillation. *J. Climate*, **12**, 1918–1939.

Wheeler, M., and G. N. Kiladis, 1999: Convectively coupled equatorial waves: Analysis of clouds and temperature in the wavenumber-frequency domain. *J. Atmos. Sci.*, **56**, 374–399.

———, ———, and P. J. Webster, 2000: Large-scale dynamical fields associated with convectively coupled equatorial waves. *J. Atmos. Sci.*, **57**, 613–640.

List of Figures

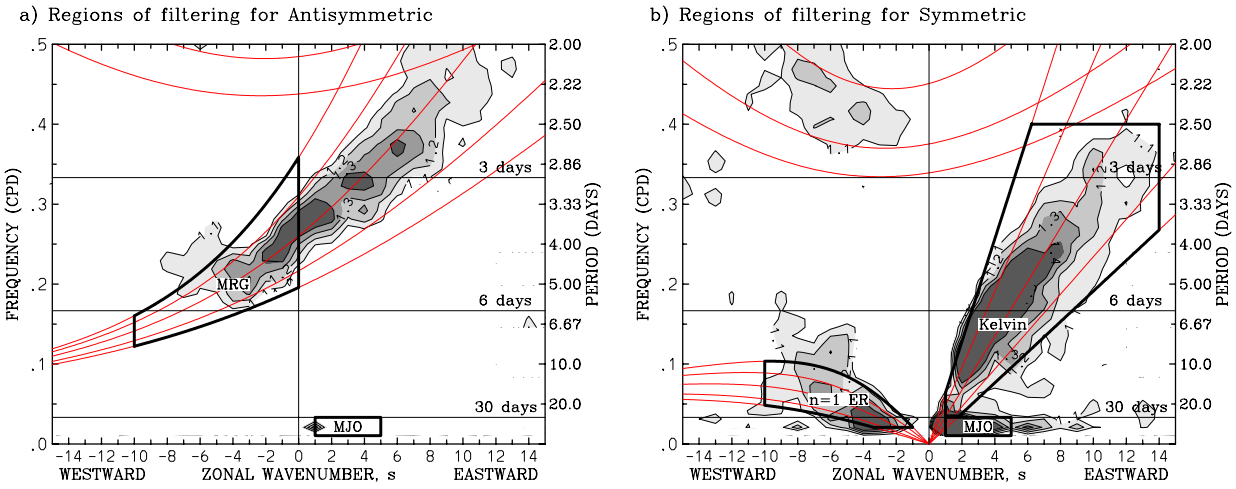

FIG. 1: Regions of wavenumber-frequency filtering (thick boxes) used to obtain the time-longitude information of the modes of coherent tropical variability for the (a) antisymmetric component and (b) symmetric component of the field with respect to the equator. These regions overlie the spectral peaks (the contours and shading) of the convectively coupled waves as identified in the analysis of many years (1979-1996) of outgoing longwave radiation (OLR) data in WK99. The thin lines are the various equatorial wave dispersion curves for the equivalent depths of $h = 8, 12, 25, 50$ and 90 m. For more details, see Section 3.

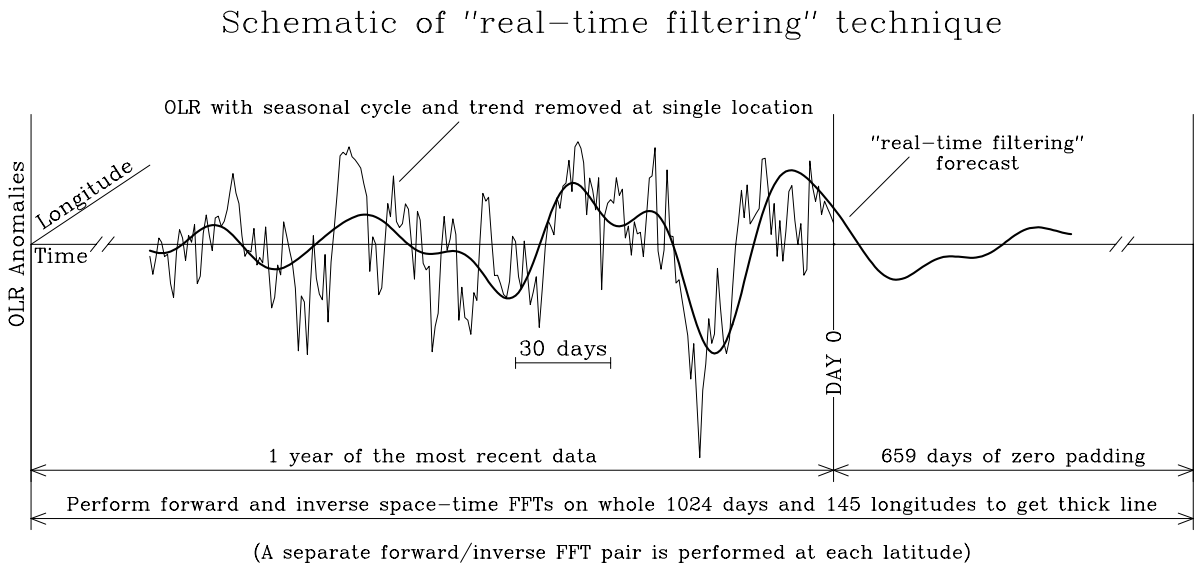

FIG. 2: Schematic of the procedure of real-time filtering for monitoring and prediction, as applied to a time series with an MJO-like signal.

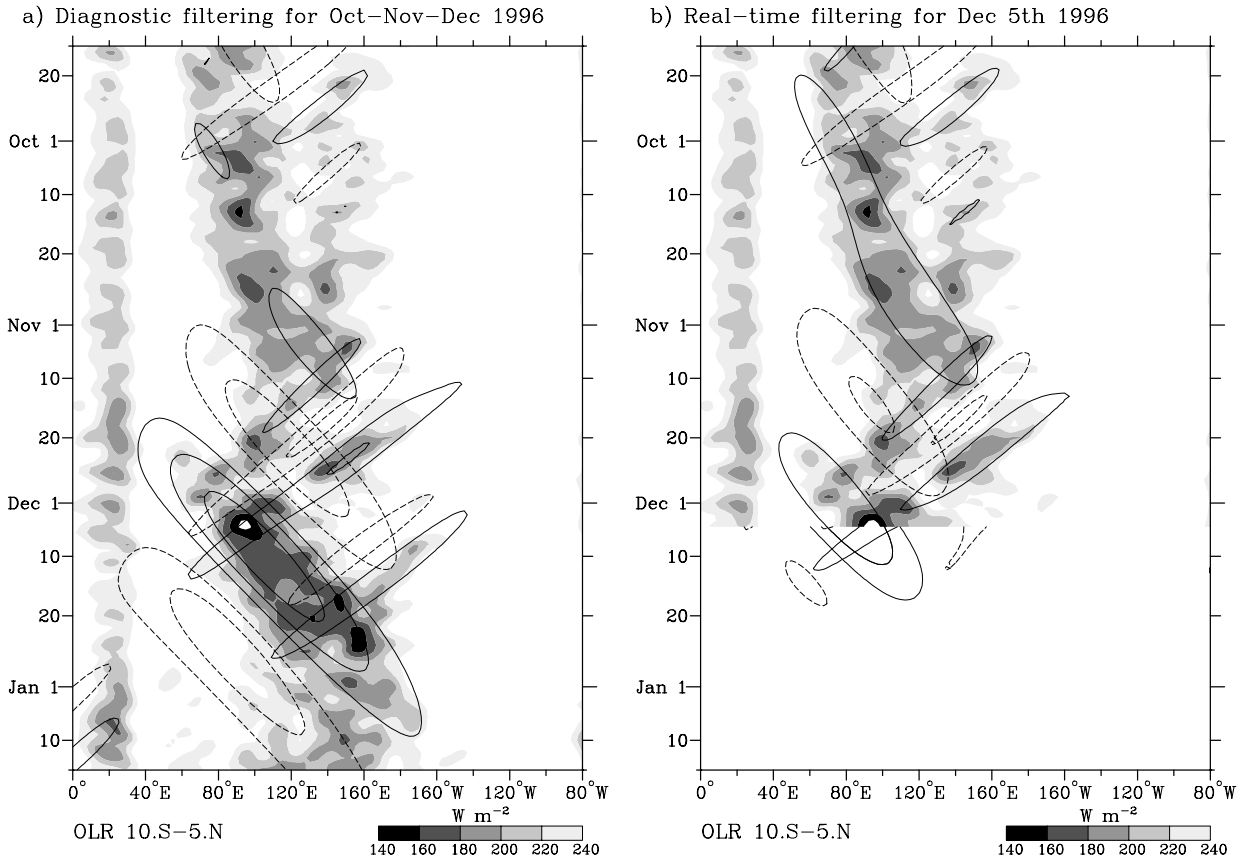

FIG. 3: (a) Time-longitude plot of the total OLR (with R21 spatial truncation, and a 1-2-1 filter applied in time) and filtered OLR anomalies averaged between 10°S and 5°N during late 1996 to early 1997. Shading is for the total OLR, and contours are for the diagnostically-filtered anomalies of the MJO and $n = 1$ equatorial Rossby (ER) wave. Solid contours represent negative OLR anomalies, while dashed contours are for positive anomalies, with the contour interval for both wave filtered bands being 10 W m^{-2}, and the zero contour omitted. (b) Same as (a), except that the filtering was performed with the last day of data being on December 5th, 1996. After December 5th, when the real-time filtered anomalies are continued into the future as a forecast, the contour interval is halved.

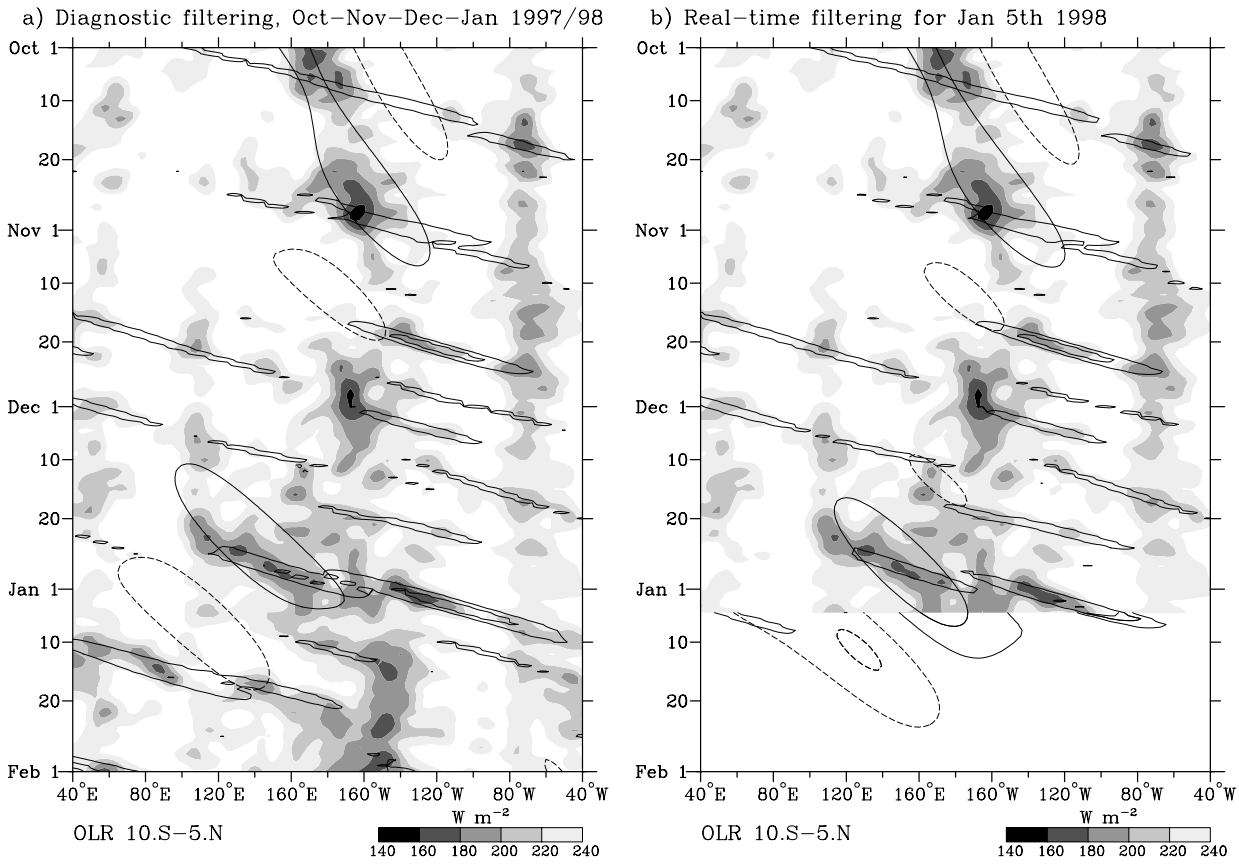

FIG. 4: (a) Same as Fig. 3a, except for the 1997/1998 period, and the MJO and Kelvin wave filtering are displayed. The range of longitudes has also been shifted by 40°. Contour interval for the MJO filtered anomalies is 10 W m^{-2}, and for the Kelvin wave anomalies is 15 W m^{-2}. Positive contours of the Kelvin wave anomalies are omitted. (b) Same as Fig. 3b, except for the real-time filtering of the 5th January, 1998, and only the MJO and Kelvin wave anomalies are displayed.

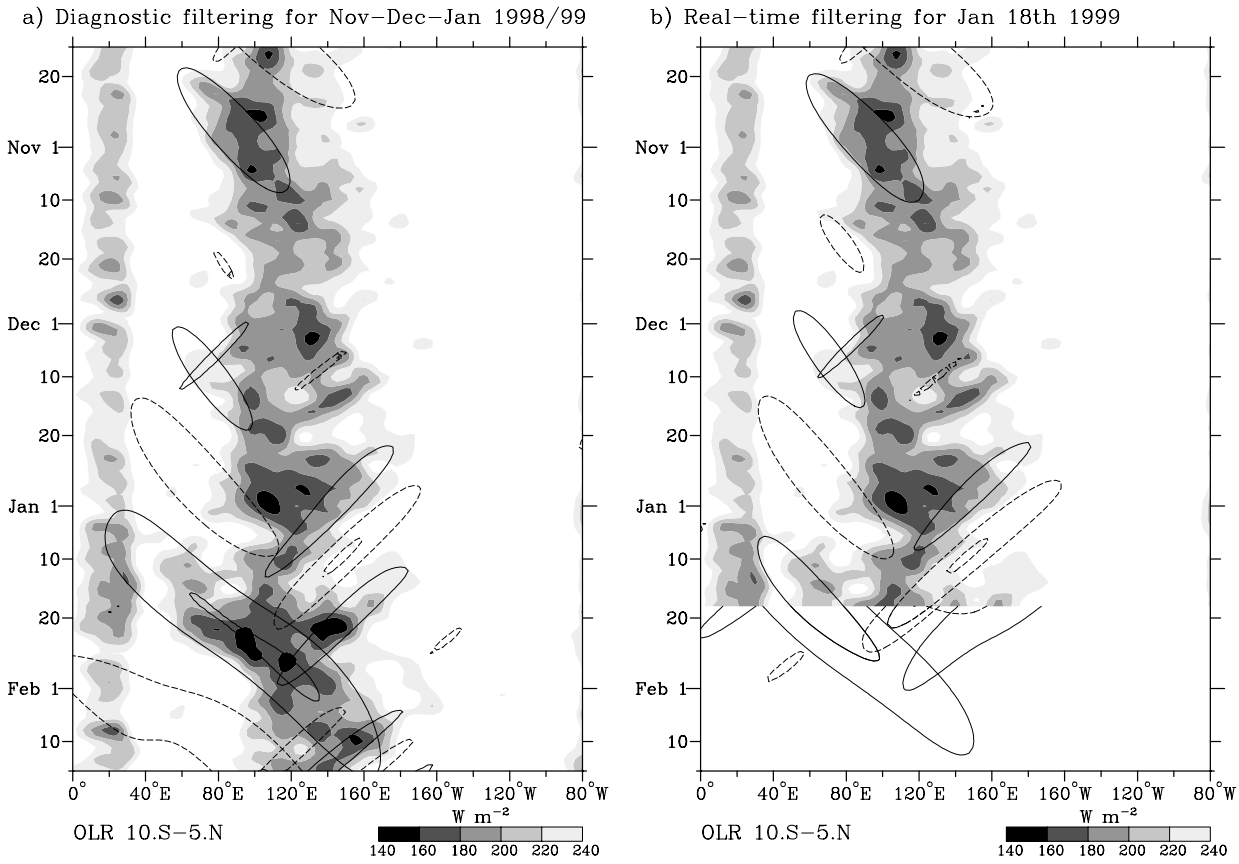

FIG. 5: (a) Same as Fig. 3a, except for the 1998/1999 period. (b) Same as Fig. 3b, except for the real-time filtering of the 18th January, 1999.

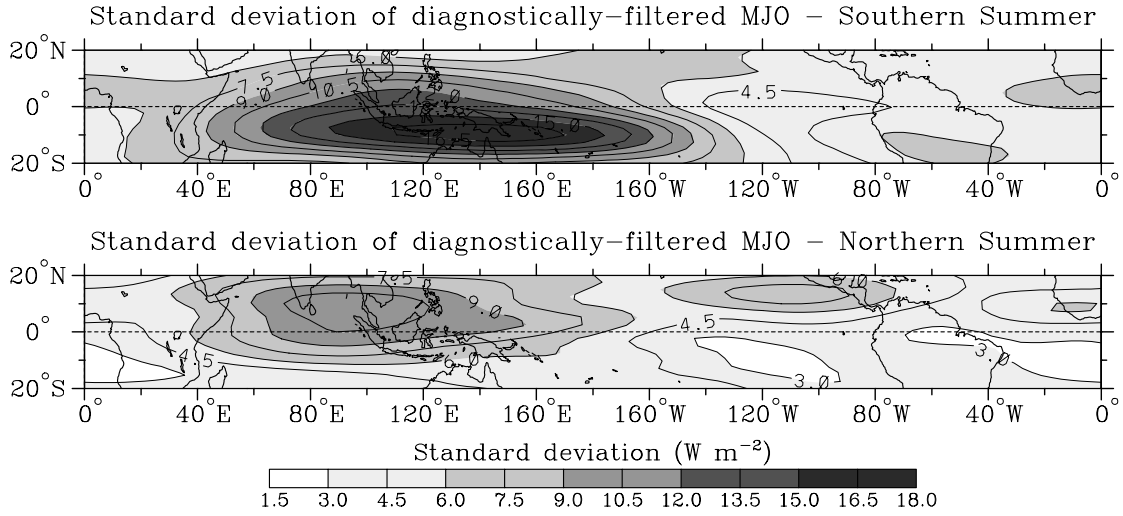

FIG. 6: Standard deviation of the diagnostically-filtered MJO OLR for the 10-year period of 1985 to 1994, separately for southern summer (above) and Northern summer (below).

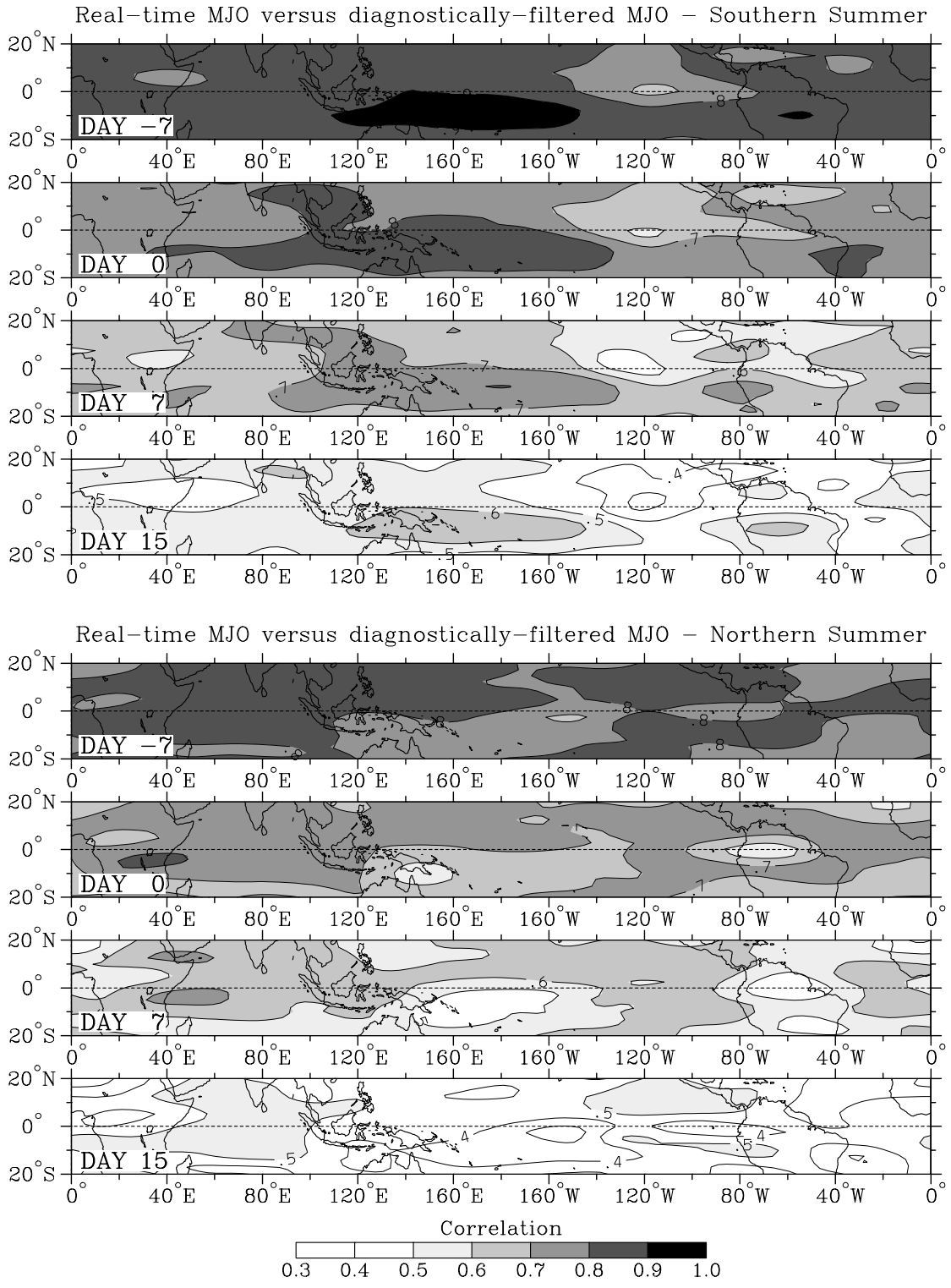

FIG. 7: Correlations of the MJO real-time filtered OLR with the validating diagnostically-filtered MJO OLR for southern summer (upper panels) and Northern summer (lower panels), for a number of lead times in days. Lead time is with respect to the end-point of the data input into the real-time filtering procedure as indicated in the lower left of each panel. All 10 years of the sample forecasts were used.

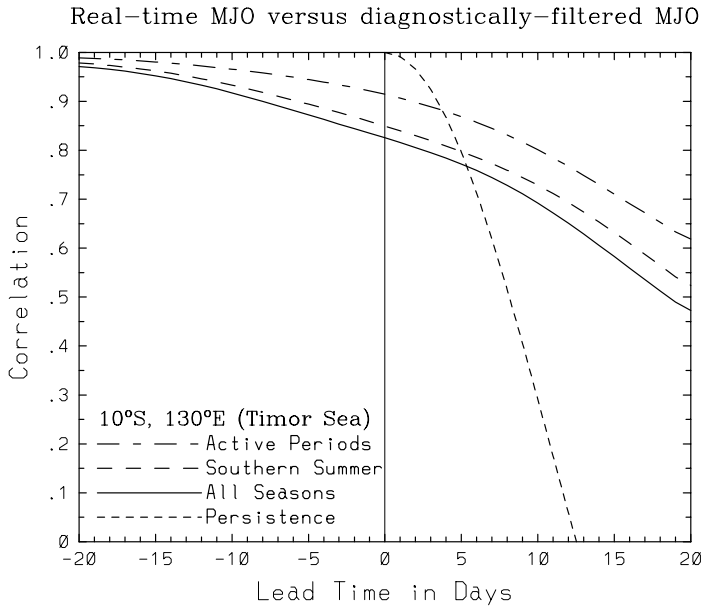

FIG. 8: Correlations of the MJO real-time filtered OLR with the validating diagnostically-filtered MJO OLR at the point 10°S, 130°E as a function of lead time. The correlations were calculated using all seasons, southern summer only, and "active" periods only of the 10 years of sample forecasts, as labeled. Additionally shown are correlations for a persistence forecast with the diagnostically-filtered MJO OLR at this point, equivalent to its autocorrelation function at this point. Note that this "persistence forecast" can not be performed in real time.

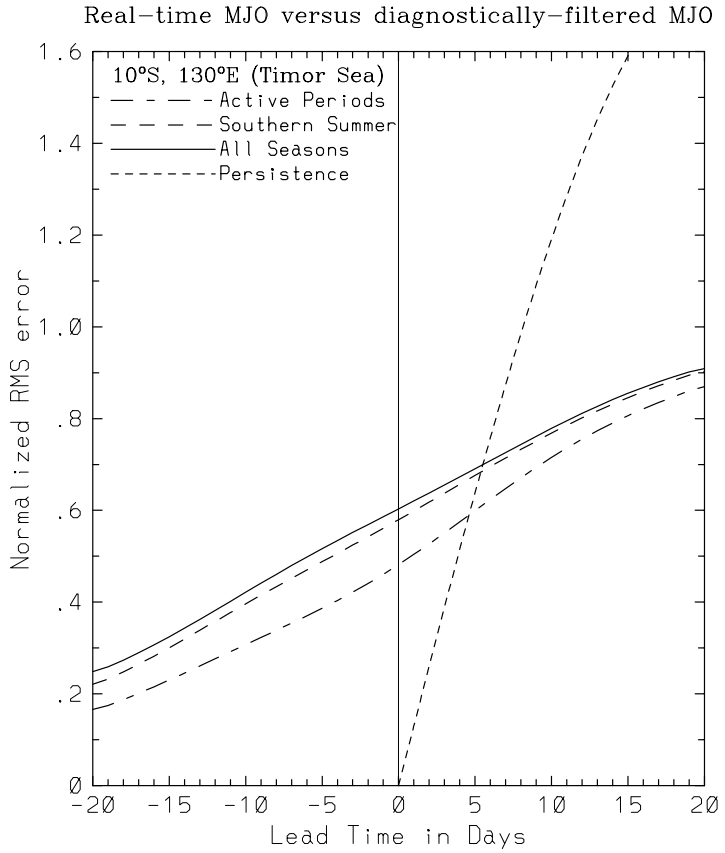

FIG. 9: As in Fig. 8, except for the normalized rms error between the real-time filtered MJO OLR and the diagnostically-filtered MJO OLR at the point 10°S, 130°E. Also shown is the normalized rms error for a persistence (of the diagnostically-filtered field) forecast. Note that this "persistence forecast" can not be performed in real time.

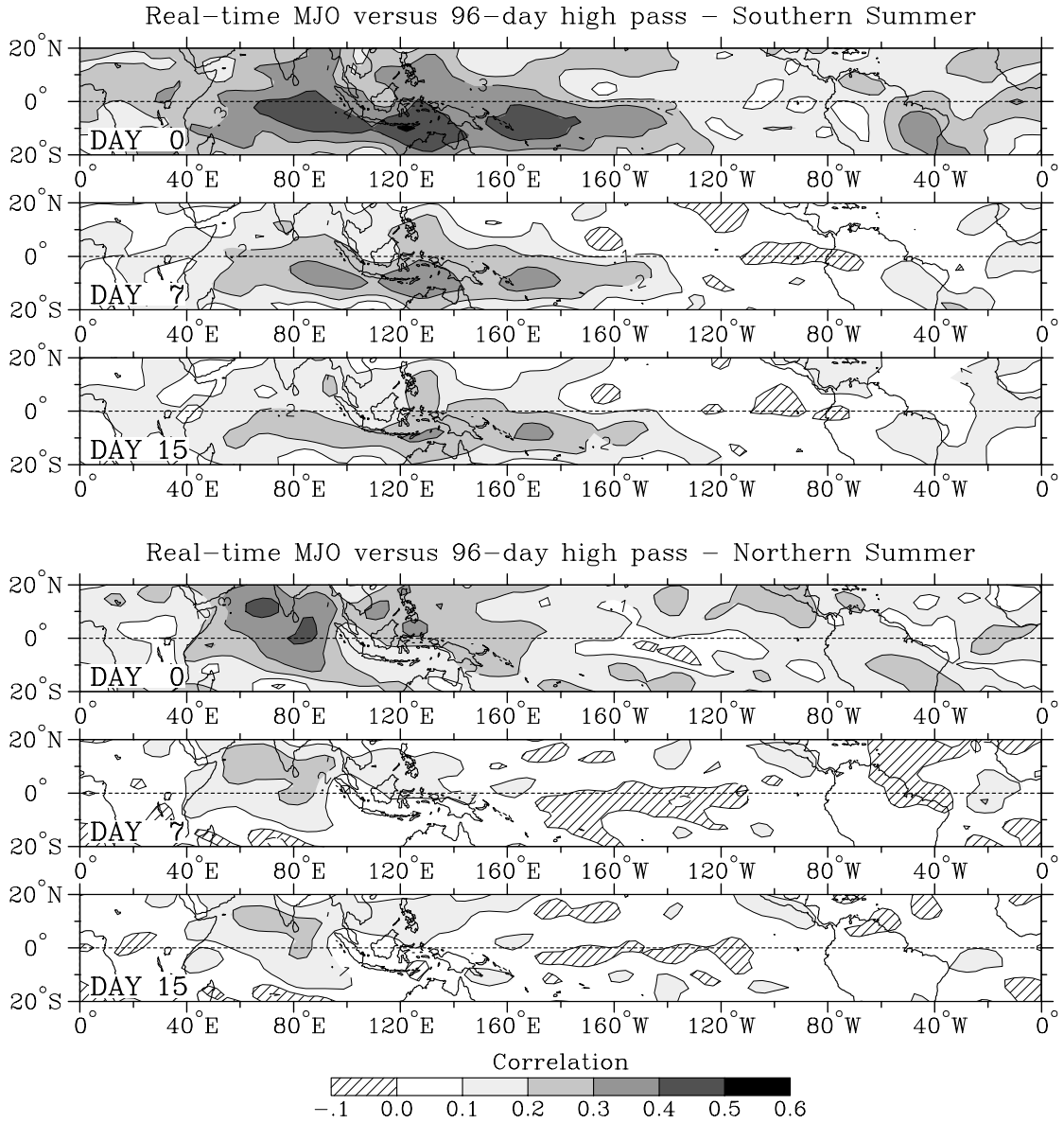

FIG. 10: As in Fig. 7, except for the correlation between the real-time filtered MJO OLR and the corresponding 96-day high-pass OLR anomalies.

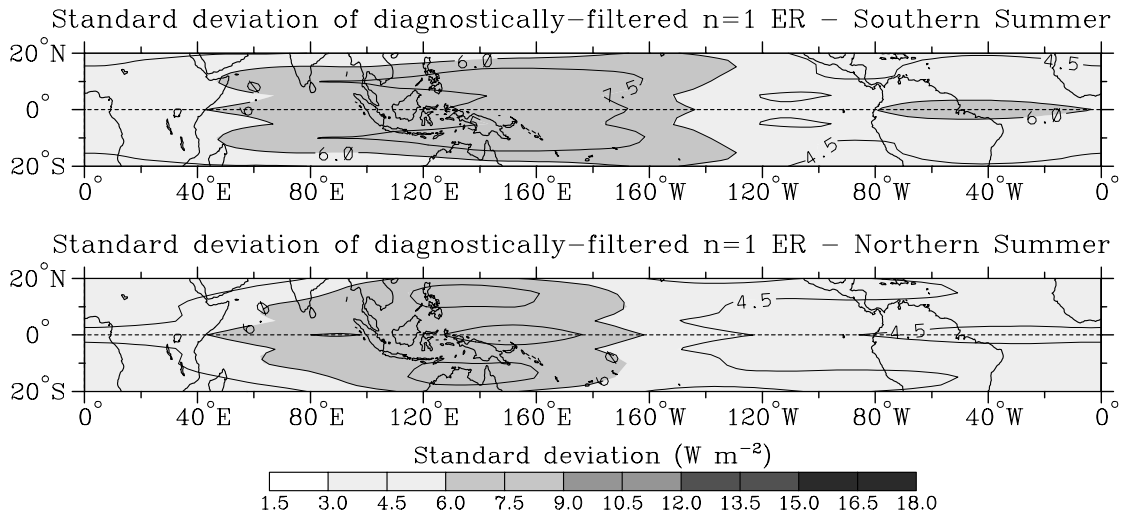

FIG. 11: As in Fig. 6, except for the $n = 1$ ER wave.

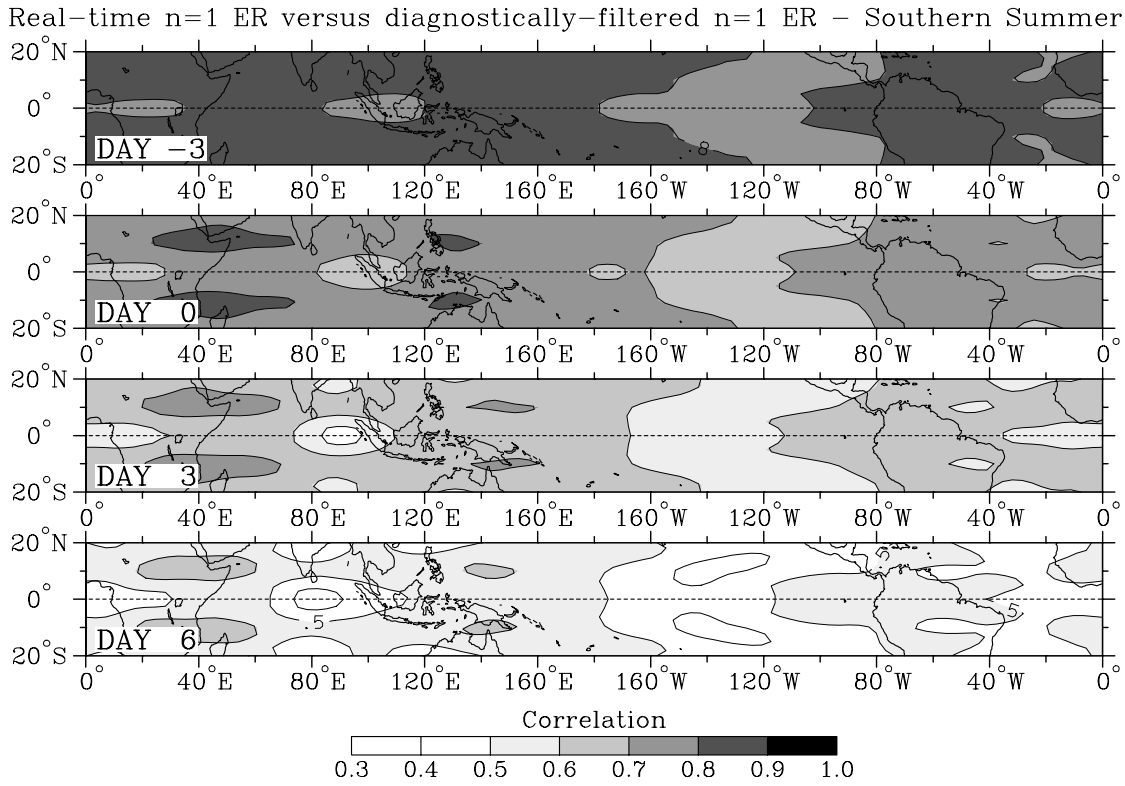

FIG. 12: As in Fig. 7, except for the correlations of the $n = 1$ ER wave real-time filtered OLR for southern summer only.

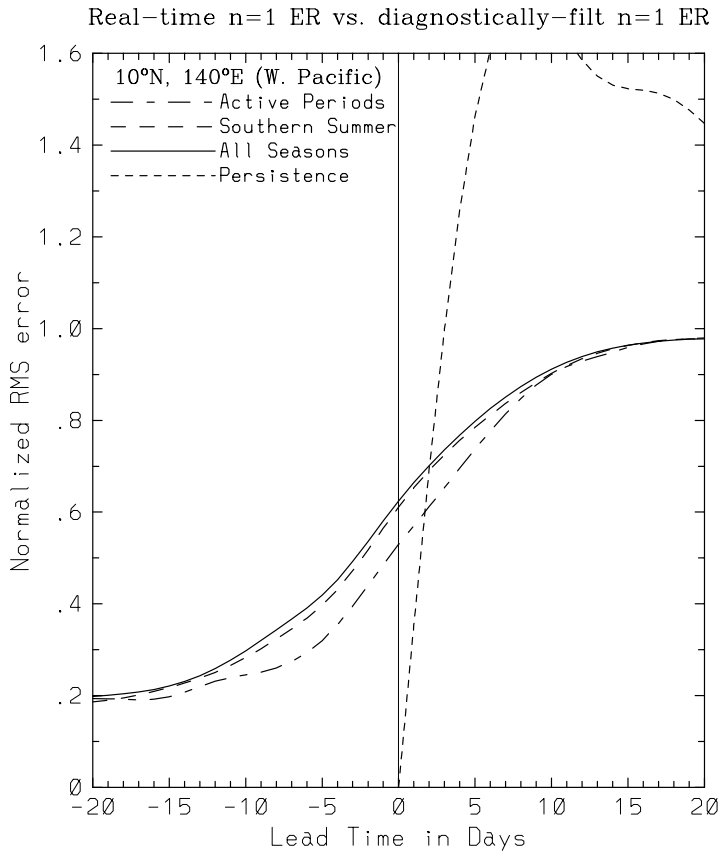

FIG. 13: As in Fig. 9, except for the $n = 1$ ER wave OLR real-time filtering at the point 10°N, 140°E.

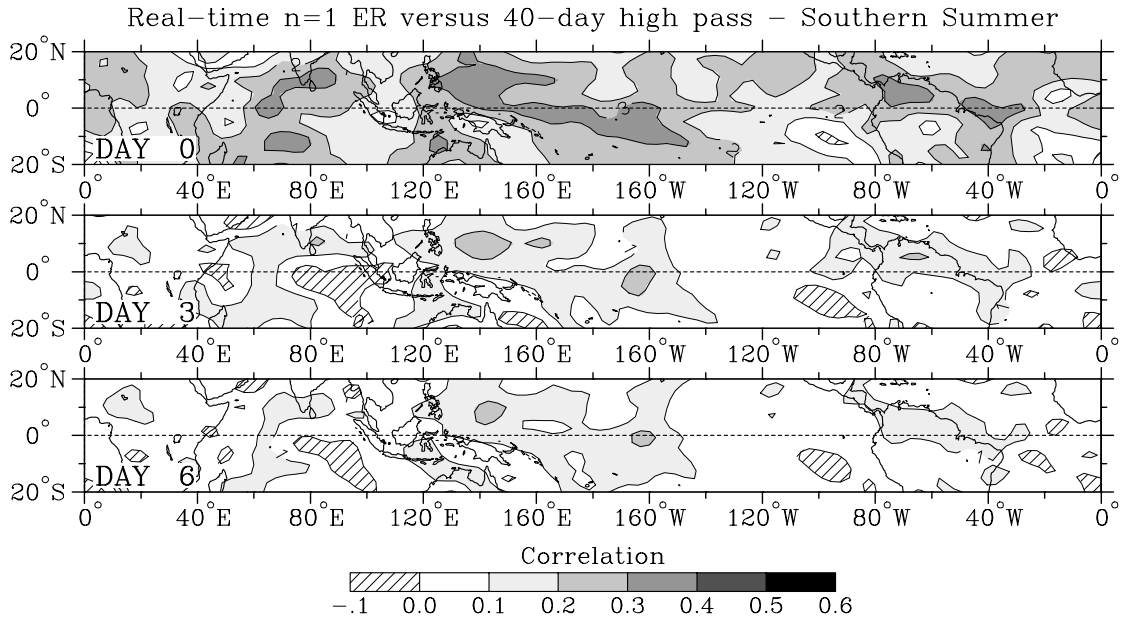

FIG. 14: As in Fig. 10, except for the correlations of the $n = 1$ ER wave real-time filtered OLR against the corresponding 40-day high-pass OLR for southern summer only.

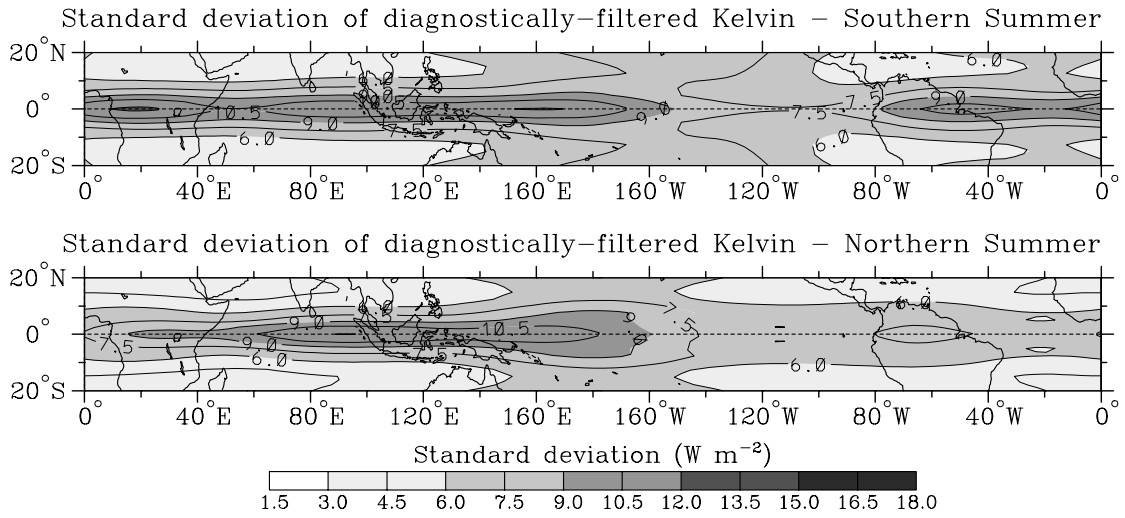

FIG. 15: As in Fig. 6, except for the Kelvin wave.

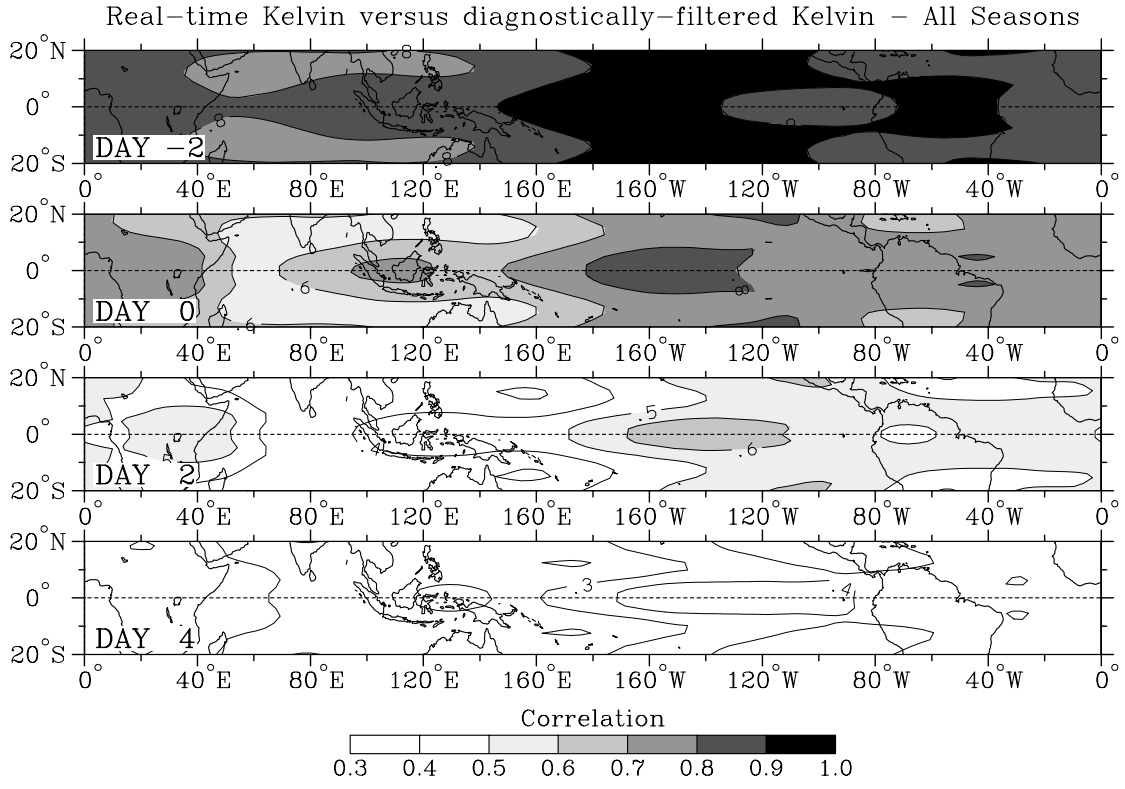

FIG. 16: As in Fig. 7, except for the correlations of the Kelvin wave real-time filtered OLR for all seasons.

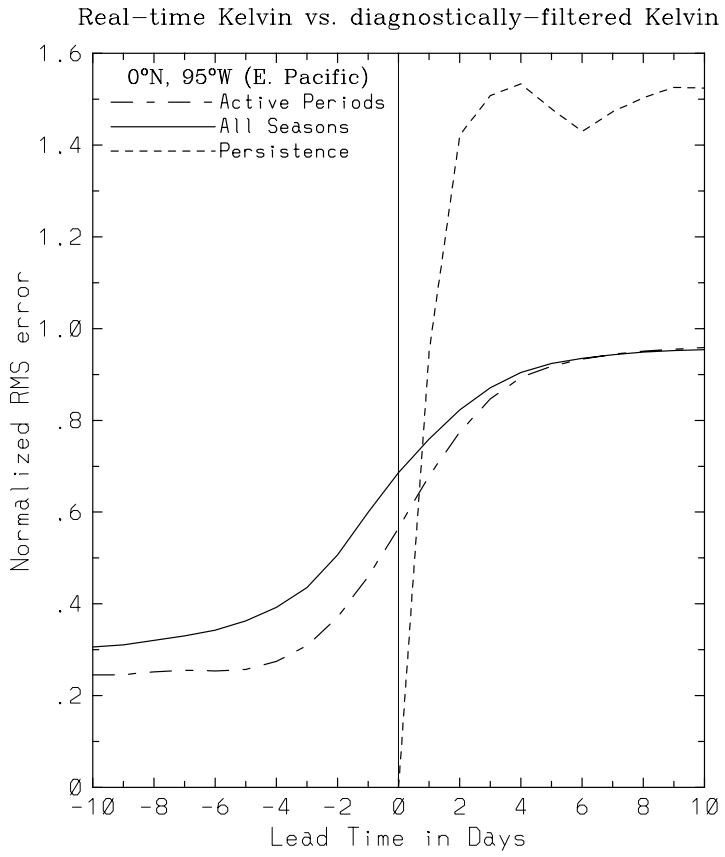

FIG. 17: As in Fig. 9, except for the Kelvin wave OLR real-time filtering at the point 0°N, 95°W.

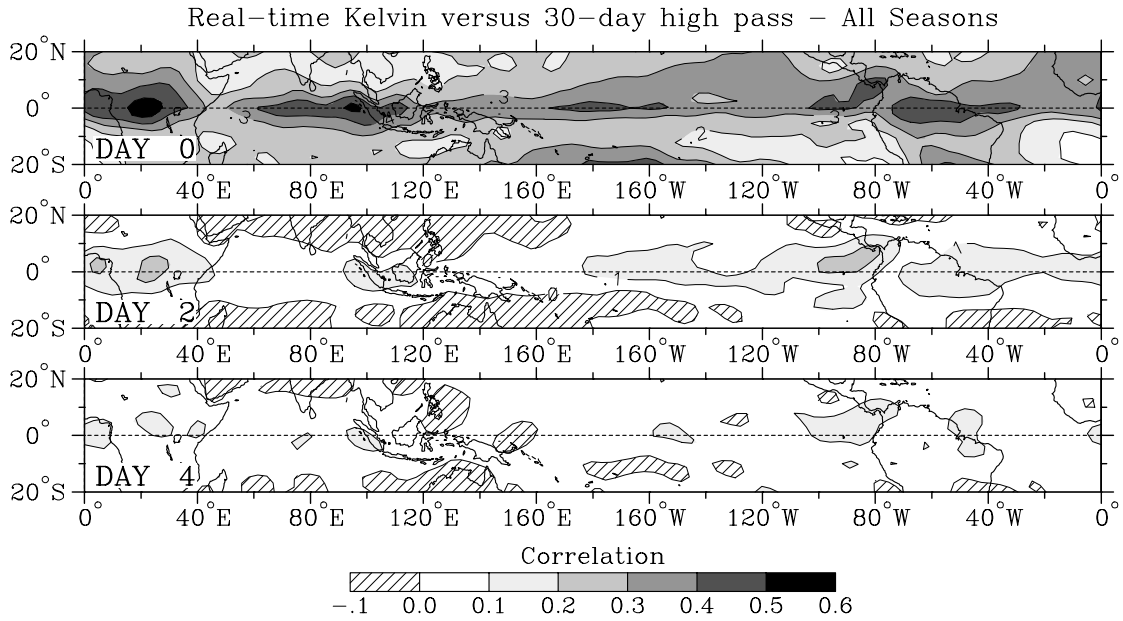

FIG. 18: As in Fig. 10, except for the correlations of the Kelvin wave real-time filtered OLR against the corresponding 30-day high-pass OLR for all seasons.

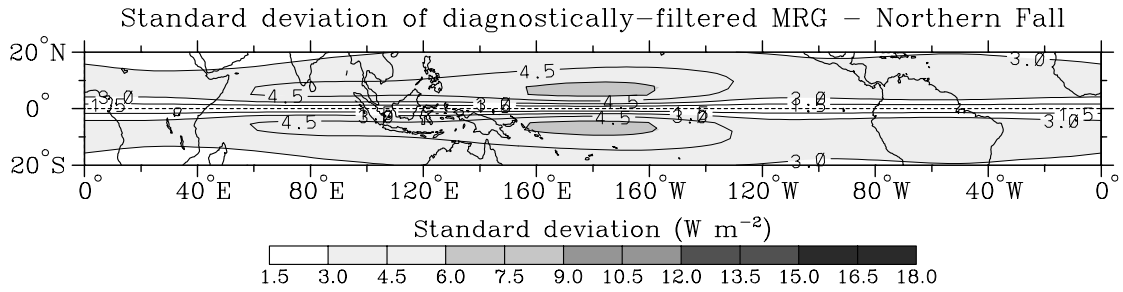

FIG. 19: As in Fig. 6, except for the MRG wave, and for the season of Northern fall (defined as August to January) only.

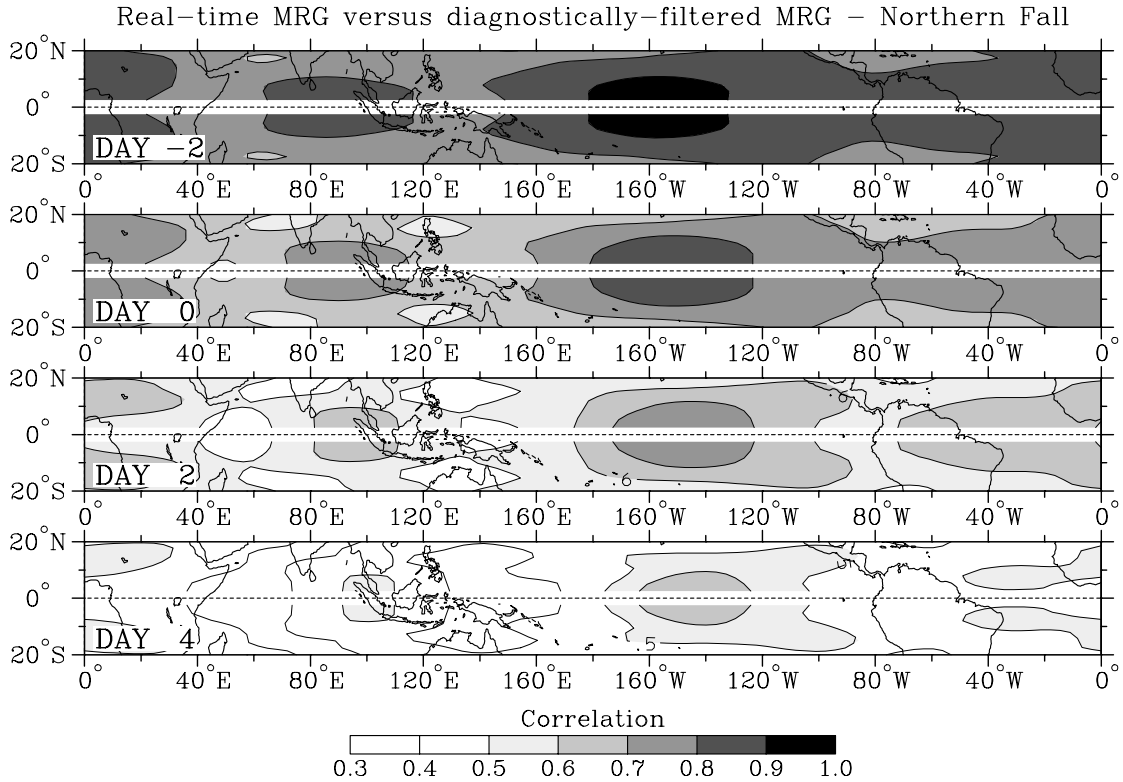

FIG. 20: As in Fig. 7, except for the correlations of the MRG wave real-time filtered OLR for Northern fall only. The correlation is not shown at the equator as the defined antisymmetric OLR field of the MRG waves is zero there.

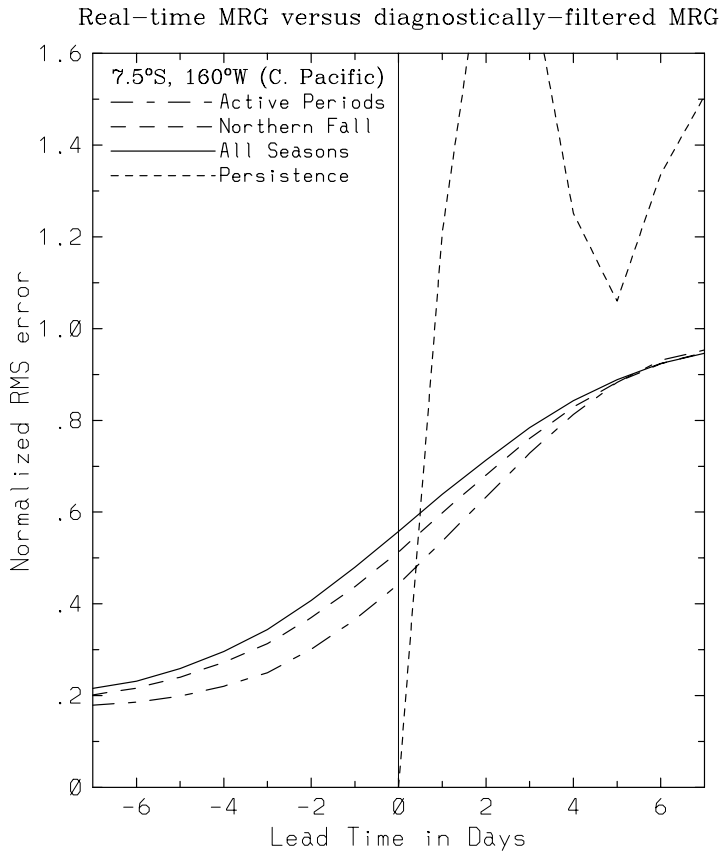

FIG. 21: As in Fig. 9, except for the MRG wave OLR real-time filtering at the point 7.5°S, 160°W.

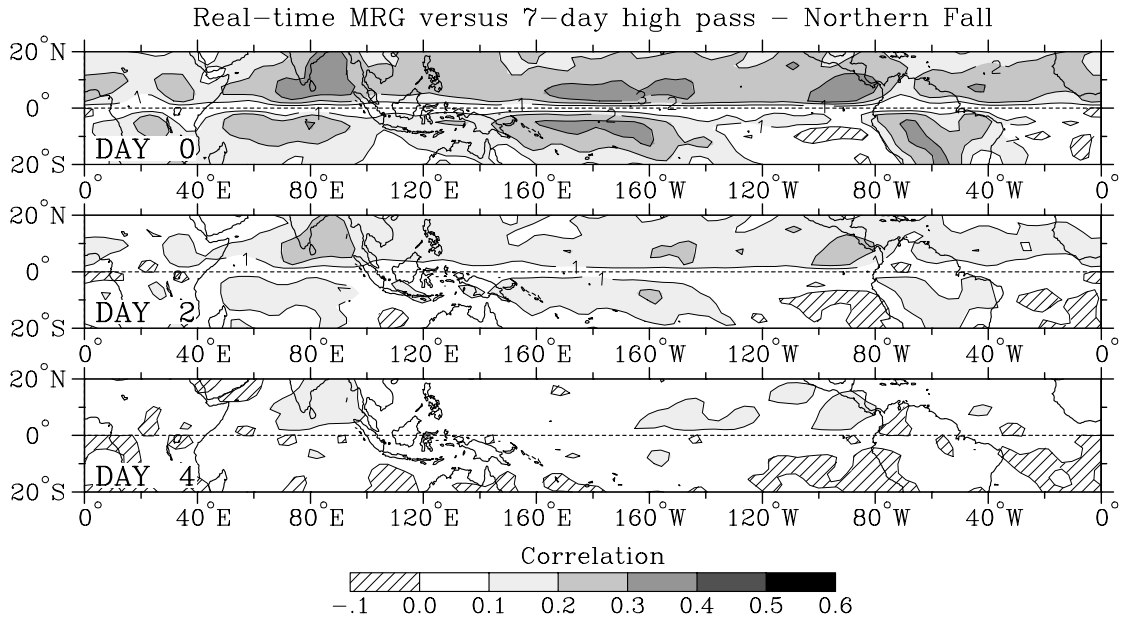

FIG. 22: As in Fig. 10, except for the correlations of the MRG wave real-time filtered OLR against the corresponding 7-day high-pass OLR for Northern fall only.

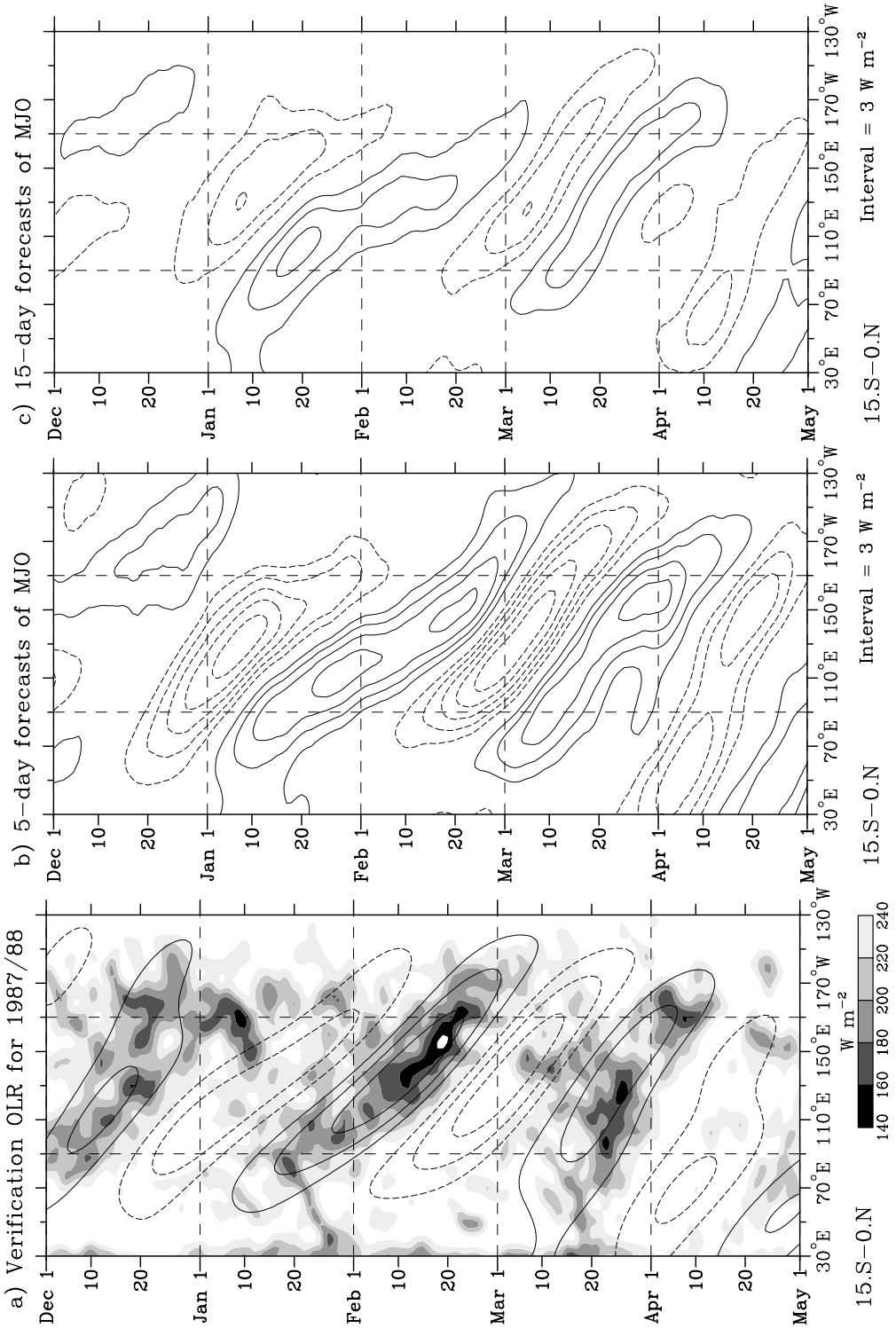

FIG. 23: (a) As in Fig. 3a except for the period, latitudes, and longitudes as specified. Contour interval for the diagnostically-filtered MJO OLR anomalies is 10 W m^{-2}. (b) Time-longitude plot of the 5-day real-time filtering forecasts of the MJO OLR that verify on the days as specified. (c) As in (b) except for the 15-day forecasts of the MJO OLR. Contour interval for (b) and (c) is as specified with positive contours dashed.

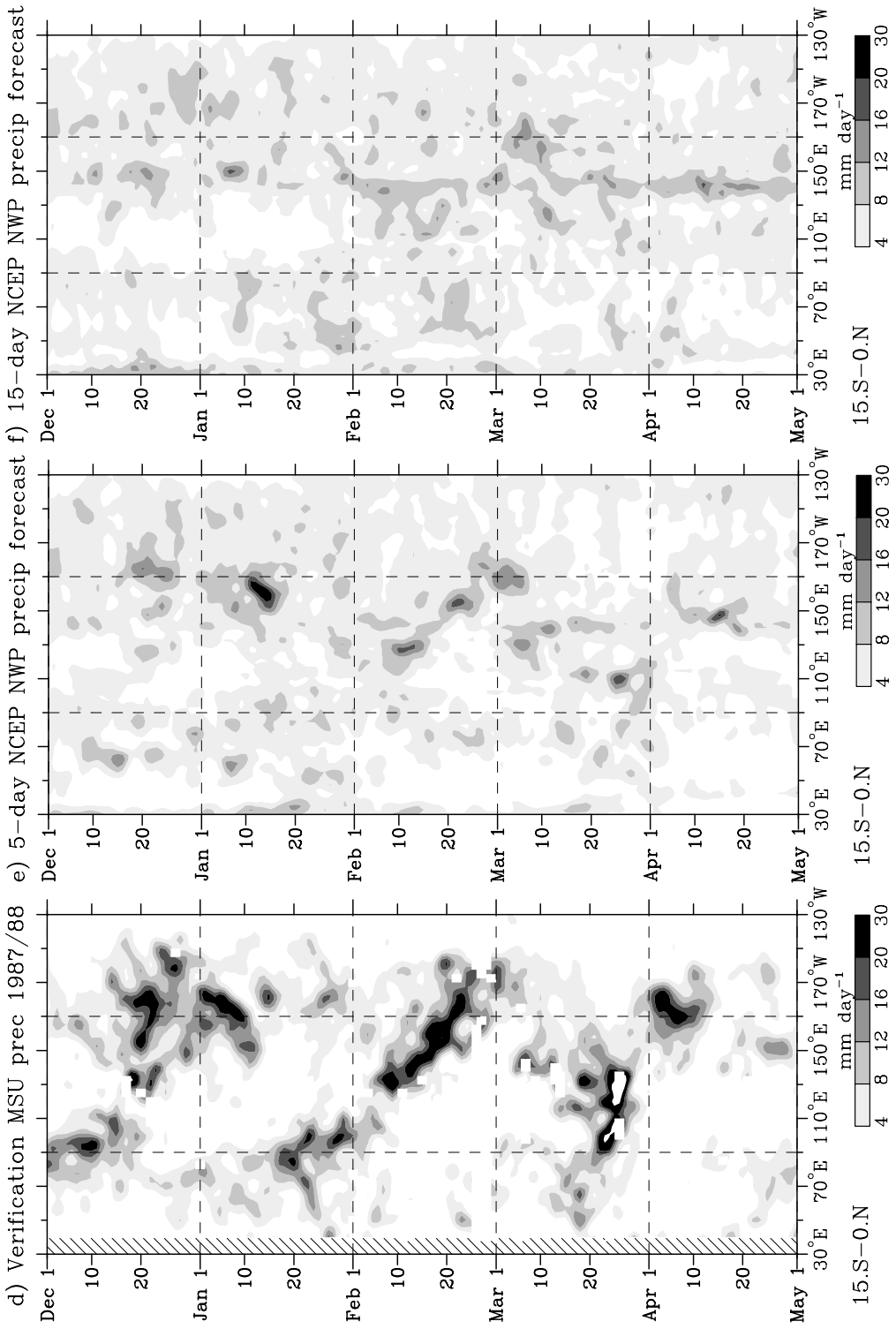

FIG. 23: (*Continued*) (d) Time-longitude plot of the verifying MSU precipitation. Missing data is left blank and land areas hatched. Spatial and temporal smoothing applied to mimic R21 truncation and temporal smoothing of the OLR in (a). (e) as in (b) except for the 5-day forecasts of precipitation from the NCEP model in mm day^{-1}. Spatial smoothing applied to match (a). (f) as in (e) except for the 15-day forecasts.

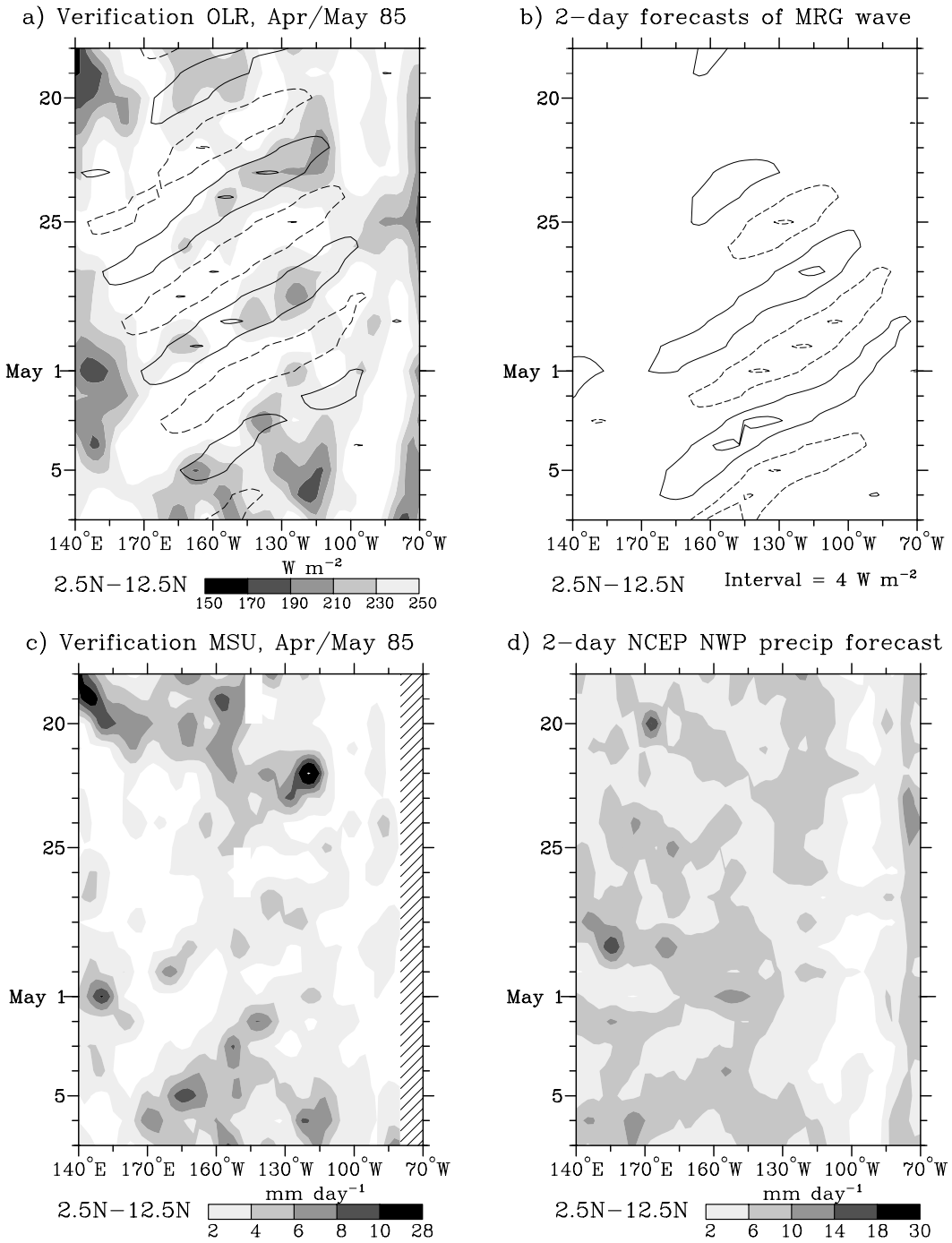

FIG. 24: (a) As in Fig. 23a except for the period, latitudes and longitudes as specified, showing the MRG wave diagnostic filtering, and without a 1-2-1 filter applied in time. Contour interval for the MRG wave filtering is 7 W m^{-2}. (b) Time-longitude plot of the 2-day real-time filtering forecasts of the MRG wave OLR that verify on the days as specified. Contour interval is as specified. (c) Time-longitude plot of the verifying MSU precipitation. Missing data is left blank and land areas hatched. Spatial smoothing applied to mimic that of the OLR in (a). (d) as in (b) except for the 2-day forecasts of precipitation from the NCEP model in mm day^{-1}, and spatial smoothing applied to match (a).